Section 5

PHOTONICS

Optical Models of Organic Light Emitting Devices

K. Celebi, T.D. Heidel, M.A. Baldo
Sponsorship: DARPA, NSF NIRT

We calculate the dipole energy propagation in a multilayer stack by analytically extending the theoretical model of Chance, Prock and Silbey [1], which calculates the field pattern and lifetime of a dipole in this geometry. This analytical extension [2] facilitates numerical calculations to predict the outcoupling and optical dissipation mechanisms of an organic light emitting device (OLED), where the excitons can be modeled as dipoles. We have applied this approach to a previous experimental measurement of an OLED outcoupling by Segal *et al.* [3] The model predictions agree with the experiment, yielding a similar outcoupling efficiency, and in addition shows the mode-resolved spatial dipole energy dissipation of the same device (Figure 1). Thus we conclude that the surface-parallel oriented dipoles generate most of the emitted light, and the main optical loss mechanisms are the waveguiding in the glass and organic layers, along with a smaller loss to the plasmon modes of the cathode. Our method can be used for designing low-loss OLED structures and efficient cavity designs.

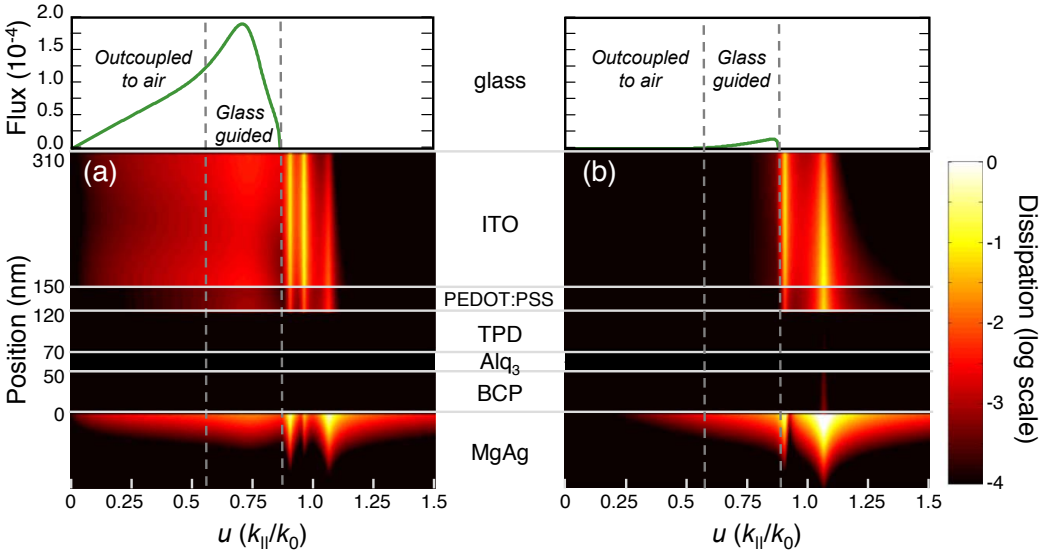

▲ Figure 1: (a) Absorption of the parallel dipole energy as a function of the position and normalized surface-parallel wave vector. The dipole is located at the middle of the Alq_3 layer and the emission wavelength is λ = 535 nm. Bright features correspond to a higher absorption. The green curve shows the outcoupled energy flux. (b) Same absorption as in part (a) but for perpendicular dipole. Perpendicular dashed lines divide this flux into air-outcoupled, glass-waveguided, organics-waveguided and surface plasmon polariton (SPP) portions. At λ = 535 nm, the dielectric constants for Mg, BCP, Alq_3, TPD, PEDOT and ITO are the following: $\varepsilon = 1.908 + 0.265i$, $\varepsilon = 2.985 + (4.11 \times 10^{-5})i$, $\varepsilon = 2.962$, $\varepsilon = 2.985 + (4.11 \times 10^{-5})i$, $\varepsilon = 2.304 + (3.33 \times 10^{-2})i$ and $\varepsilon = 3.295 + (3.63 \times 10^{-2})i$, respectively. Note that the dielectric constant of TPD was assumed to be equal that of BCP. (Figure is taken from [2]).

REFERENCES

[1] R.R. Chance, A. Prock and R. Silbey, "Molecular fluorescence and energy transfer near metal interfaces," in *Advances in Chemical Physics Vol. 37*, I. Prigogine and S. A. Rice, Eds. New York. NY: Wiley, 1978.

[2] K. Celebi, T.D. Heidel, and M.A. Baldo, "Simplified calculation of dipole energy transport in a multilayer stack using dyadic Green's functions," *Optics Express*, vol. 15, pp. 1762-1772, Feb. 2007.

[3] M. Segal, M.A. Baldo, R.J. Holmes, S.R. Forrest, and Z.G. Soos, "Excitonic singlet-triplet ratios in molecular and polymeric organic materials," *Physical Review B*, vol. 68, pp. 075211:1-14, Aug 2003.

Electric Field and Temperature Dependent Analytic Model of Charge Carrier Mobility in Amorphous Organic Semiconductors

B.N. Limketkai, P.J. Jadhav, M.A. Baldo
Sponsorship: DuPont, MIT

Understanding the electric-field dependence of charge carrier mobility is central to the rational design of organic semiconductor devices [1]. Studies of charge transport in organic semiconductors have observed a log $\mu \sim \sqrt{F}$, or Poole-Frenkel, dependence of charge carrier mobility, μ, on electric field, F. Numerical simulations have established that the Poole-Frenkel dependence is due to disorder, and analytic theories have continued to employ simulation-based empirical models in efforts to jointly summarize the electric-field, temperature-, and charge-density-dependencies [1].

In this research we present a complete analytic description of mobility by considering non-equilibrium carrier distributions within a percolation framework. Only three free parameters are required: the width of the density of states, the decay length of the charge carrier wavefunction, and the maximum conductivity, which depends in turn on the strength of the intermolecular interaction. The electric field dependence of charge carrier mobility is found to be well-modeled by an effective temperature, suggesting that the dominant effect of the electric field is to generate a nonequilibrium charge carrier distribution.

The theory is compared to measurements by Brütting, *et al* [1] of the current-voltage and mobility of the archetype small molecule tris (8-hydroxyquinoline) aluminum. The theory accurately reproduces the temperature, carrier density, and electric field dependencies of the experimental data over a wide range of temperatures, carrier densities, and electric fields. Most significantly, the mobility theory enables predictive models of organic semiconductor devices based on material parameters that may be determined by *ab initio* quantum chemical simulations. Consequently, we expect that the theory will allow the rational design of organic devices in important applications such as video displays and solar cells.

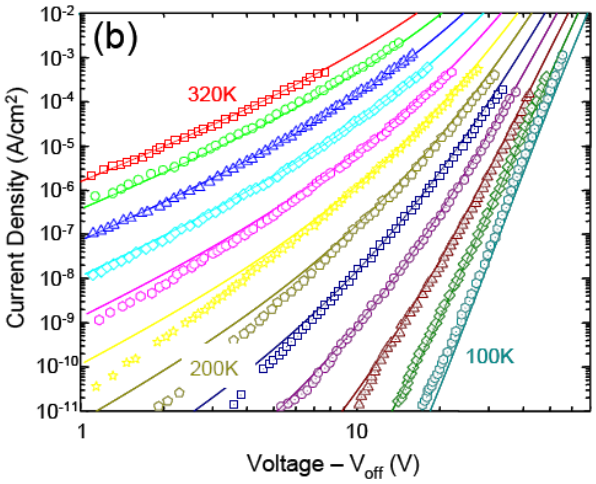

▲ Figure 1: Temperature-dependence of the *J-V* characteristics of an Al/Alq3/Ca device with an Alq3 thickness of 300 nm[1]. Solid lines show theoretical fits. Current-voltage curves were offset by a voltage *Voff* = 2V to compensate for uncertainty in *Vbi* and the contact resistances.

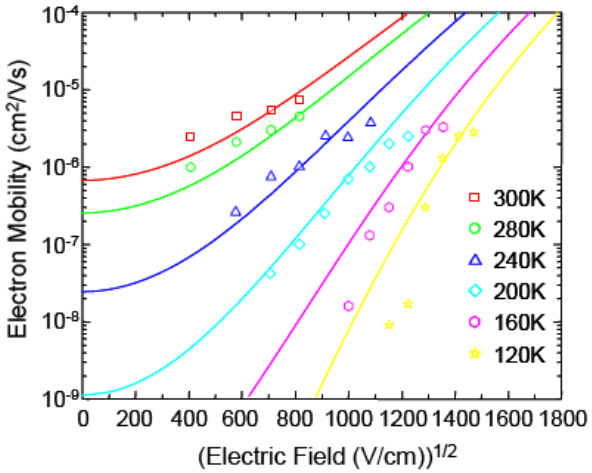

▲ Figure 2: Temperature and electric field dependence of charge carrier mobility obtained from transient electroluminescence measurements [1]. Theoretical fits are shown in solid lines.

REFERENCES

[1] W. Brütting, S. Berleb, and A.G. Mückl, "Device physics of organic light-emitting diodes based on molecular materials," *Organic Electronics*, vol. 2, no. 1, pp. 1-36, Mar. 2001.

Saturated and Efficient Blue Phosphorescent Organic Light Emitting Devices with Lambertian Angular Emission

C.L. Mulder, K. Celebi, M.A. Baldo
Sponsorship: NSF

The realization of stable blue phosphorescent organic light emitting devices (OLEDs) has proved challenging. An important limitation is the broad photoluminescent (PL) spectrum characteristic of organic dyes. For example, greenish-blue or "sky-blue" phosphors have strong emission in the blue [1]. But optical transitions to higher vibrational modes of the electronic ground state extend their emission spectrum deep into the green. Because the eye responds strongly at green wavelengths, this broad emission spectrum yields an unsaturated color that is ill suited for most display applications.

In this work a strong microcavity is employed to optimize the color of a phosphorescent organic light emitting device (OLED) based on the sky blue phosphor FIrpic. The usual disadvantages of a strong microcavity, namely the introduction of an angular dependence to the OLED's color and a non-Lambertian angular emission profile [2], are overcome by scattering the emitted radiation. As scattering sources, frosted glass, opal glass, and holographic diffusers are studied.

With a holographic diffuser as the scattering medium, the microcavity OLED achieves an external quantum efficiency of (5.5±0.6)%, as compared to (3.8±0.4)% for a conventional structure. The color coordinates of the microcavity OLED with holographic diffuser are (x,y) = (0.116±0.004, 0.136±0.010), with minimal angular color shift and a nearly ideal Lambertian angular emission profile.

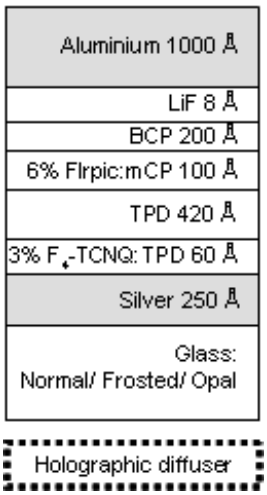

▲ Figure 1: In the strong microcavity, the anode is a thin, semitransparent layer of Ag. The cathode is Al/LiF. Devices were grown directly on the smooth back surface of frosted glass and opal glass diffusers. The holographic diffuser was employed external to devices grown on regular glass.

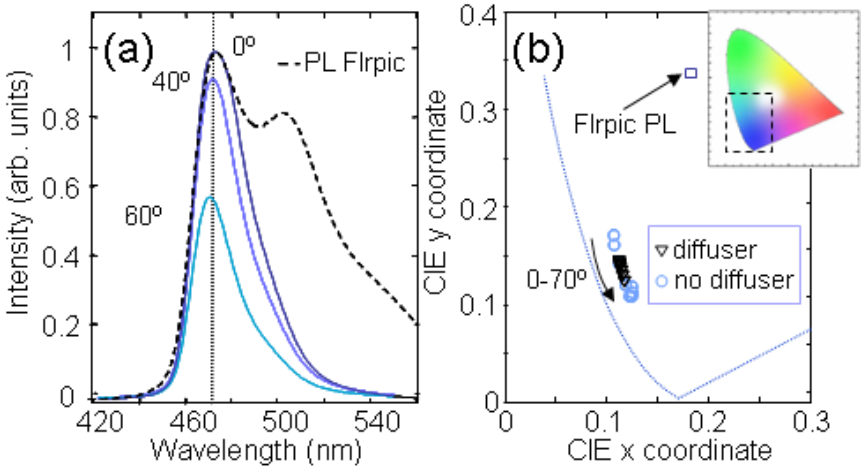

▲ Figure 2: (a) Electroluminescent spectra of the strong microcavity FIrpic OLED as a function of angle from the surface normal with the holographic diffuser. A color shift with increasing angle is barely perceptible. For comparison we plot the intrinsic photoluminescent spectrum of FIrpic (dotted line). (b) The color coordinates of the strong microcavity devices with and without holographic diffusers. Inset: the full CIE diagram identifying the expanded blue region.

REFERENCES

[1] C. Adachi, R. C. Kwong, P. Djurovich, V. Adamovich, M.A. Baldo, M.E. Thompson, and S.R. Forrest, "Endothermic energy transfer: A mechanism for generating very efficient high-energy phosphorescent emission in organic materials," *Applied Physics Letters*, vol. 79, no. 13, pp. 2082-2084, Sep. 2001.

[2] R.H. Jordan, A. Dodabalapur, and R.E. Slusher, "Efficiency enhancement of microcavity organic light emitting diodes," *Applied Physics* Letters, vol. 69, no. 14, pp. 1997-1999, Sept. 1996.

Extrafluorescent Electroluminescence in Organic Light Emitting Devices

M. Segal, M. Singh, K. Rivoire, S. Difley, T. Van Voorhis, M.A. Baldo
Sponsorship: NSF, NSERC, 3M Corporation

Organic light emitting devices (OLEDs) are a promising technology for flat panel displays and solid-state lighting due to their low cost, low power consumption, and mechanical flexibility. These OLEDs can produce two kinds of light: fluorescence, the result of an allowed transition, and phosphorescence, the result of a partly forbidden transition.[1] Fluorescent OLEDs represent the vast majority of all OLEDs and have better stability in certain colors but have efficiencies that are usually limited by spin conservation to one fourth of phosphorescent efficiencies [1]. We have demonstrated a technology for raising the efficiency of fluorescent OLEDs to approach that of phosphorescent OLEDs [2]. This should prove to be a major step forward in producing stable and high-efficiency OLEDs across all colors.

The efficiency of fluorescent OLEDs is limited by the process in which a neutral molecular excited state, or exciton, is created from oppositely-charged neighboring molecules. Excitons can have triplet or singlet spin symmetry. Typically only singlet excitons are luminescent, and they represent only 25% of all excitons formed. We demonstrate that this percentage can be increased to nearly 100% by mixing the spins of exciton precursor states. We have calculated that the singlet exciton precursor state is lower in energy than the triplet precursor state, which will favor singlet precursors and excitons if mixing of the precursor states is introduced (Figure 1). If at the same time excessive mixing of the exciton state to dark triplets is avoided, an overall efficiency enhancement can result. We demonstrate such an efficiency enhancement using the mixing molecule FIrpic and the fluorescent material DCM2 (Figure 2).

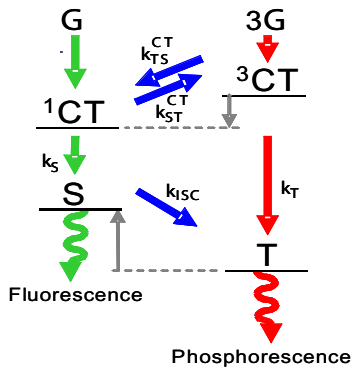

▲ Figure 1: Rate diagram for exciton formation. Triplet (^{3}CT) and singlet (^{1}CT) exciton precursor states form triplet (T) and singlet (S) excitons at rates k_S and k_T. Extrafluorescence occurs when the CT state mixing rate k_{TS}^{CT} is made large with respect to k_T, and the exciton mixing rate k_{ISC} is low. While $\Delta E_{EX} > 0$, we have calculated and measured $\Delta E_{CT} < 0$, so that $k_{TS}^{CT} > k_{ST}^{CT}$, favoring singlet production.

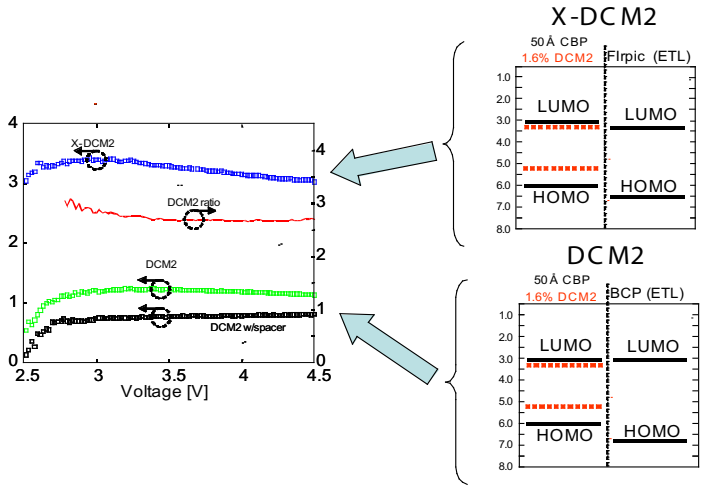

▲ Figure 2: Demonstration of an extrafluorescent OLED, or X-OLED ("X-DCM2"). The mixing molecule iridium(III) bis [(4,6-difluorophenyl) pyridinato-*N*,C$^{2'}$] picolinate (FIrpic) is used as an electron transport layer, so that exciton precursor states are preferentially mixed. The laser dye 4-(dicyanomethylene)–2–methyl–6-[(4-dimethylaninostyryl)-4-H-pyran] (DCM2) is used as an emissive material in a host of 4,4'-N,N'-dicarbazolyl-biphenyl (CBP). A control device ("DCM2") where FIrpic is replaced with 2,9-dimethyl-4,7-diphenyl-1,10-phenanthroline (BCP), which has low mixing rates, shows a 2.7× lower efficiency. A second control device ("DCM2 w/ spacer"), wherein the FIrpic layer is moved away from the emissive zone by 100 Å of BCP, shows no efficiency enhancement.

REFERENCES

[1] M.A. Baldo, D.F. O'Brien, Y. You et al., "High efficiency phosphorescent emission from organic electroluminescent devices," *Nature*, vol. 395, pp. 151-154, Sep. 1998.

[2] M Segal, M. Singh, K. Rivoire et al., "Extrafluorescent electroluminescence in organic light emitting devices," *Nature Materials*, vol. 6, pp. 374-378, Apr. 2007

Achieving Photon-number-resolution Using Multi-element Superconducting Photodetectors

E. Dauler, A.J. Kerman, B. Robinson, V. Anant, K. Rosfjord, J. Yang, K.K. Berggren
Sponsorship: USAF

We demonstrate an approach for combining multiple, independent, superconducting nanowire, single-photon detectors to create a high-speed, high-efficiency detector that can resolve photon number [1]. Optical loss in distributing the light between the elements is eliminated by fabricating a detector array with an active area identical to a single device. The scanning-electron-microscope image shown in Figure 1 illustrates one approach for subdividing a ~10 μm × 10 μm active area into four independent elements. This interleaved arrangement ensures that the light will uniformly illuminate all four elements. The fabrication [2] consists of an optical lithography and liftoff process to fabricate metal contact pads and an electron-beam lithography and reactive-ion-etching process to pattern the superconducting nanowires. The additional grating features that are not electrically connected to the detector elements are used to eliminate proximity effects in the electron-beam exposure.

To achieve high-speed photon-number-resolution, the outputs from the independent elements would typically be combined digitally, but to better illustrate the detector's photon-number resolving capabilities, we have chosen to add the analog output signals. A two-element SNSPD was illuminated with attenuated, picosecond laser-pulses and the peak voltage of the summed output was measured. A representative histogram of the measured peak voltages is shown in the inset of Figure 2. It is clear that, even with the two output pulses summed, thresholds between zero, one, and two detection events can be easily selected. The probability of each of these cases can then be measured as a function of the light intensity; Figure 2 shows these probabilities, along with calculated probabilities for the 2-element detector and an ideal photon-number-resolving detector. This approach allows the number of photons to be measured over a wide range of attenuation with a factor of ≤ 2 error due to using only two elements.

This work is sponsored in part by the United States Air Force under Air Force Contract #FA8721-05-C-0002. Opinions, interpretations, recommendations and conclusions are those of the authors and are not necessarily endorsed by the United States Government.

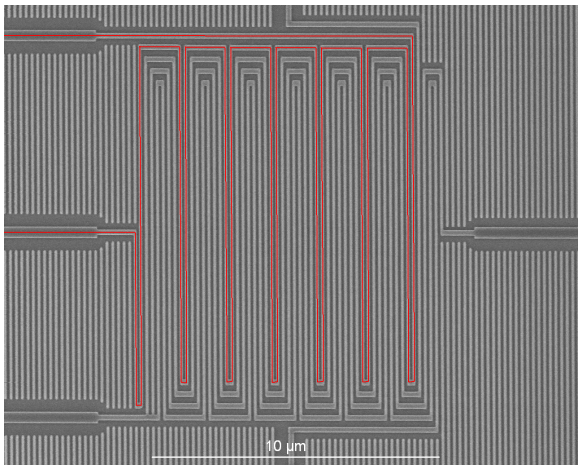

▲ Figure 1: Scanning-electron-microscope micrograph of a 4-element device with an overlaid red curve highlighting one of the four independently biased and read-out detector elements.

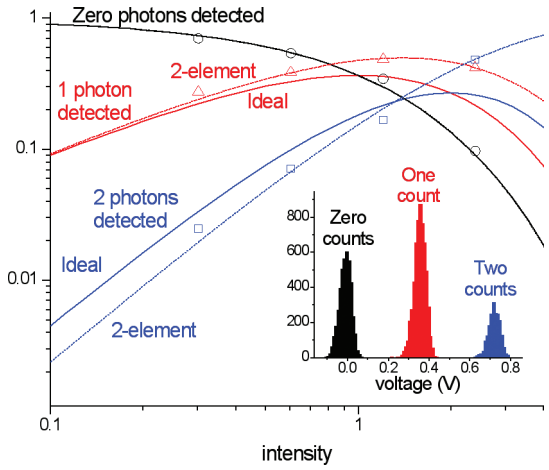

▲ Figure 2: Measured and calculated probabilities of zero, one, and two counts with an inset showing the histogram of peak voltages, colored to indicate the regions contributing to the measured probabilities.

REFERENCES

[1] E.A. Dauler, B.S. Robinson, A.J. Kerman, J.K.W. Yang, K.M. Rosfjord, V. Anant, B. Voronov, G. Gol'tsman, and K.K. Berggren, "Multi-element superconducting nanowire single-photon detector," *IEEE Transactions on Applied Superconductivity*, vol. 17, pp. 279-284, June 2007.

[2] J.K.W. Yang, E. Dauler, A. Ferri, A. Pearlman, A. Verevkin, G. Gol'tsman, B. Voronov, R. Sobolewski, W. E. Keicher, K.K. Berggren, "Fabrication development for nanowire GHz-counting-rate single-photon detectors," *IEEE Transactions on Applied Superconductivity*, vol. 15, pp. 626-620, June 2005.

Guided-wave Devices for Holographic Video Display

D. Smalley, V.M. Bove, Jr., Q. Smithwick,
Sponsorship: CELab, Digital Life, Things That Think Research Consortia, Media Laboratory

We are developing a guided-wave optical modulator [1-2] with 1 GHz composite bandwidth Surface Acoustic Wave (SAW) transducer arrays for use in video displays. This device is designed to diffract light both vertically and horizontally by creating surface acoustic waves that interact with light trapped in waveguides on the surface of a lithium niobate substrate. To fabricate this modulator, we first mask a wafer of Z-cut lithium niobate with SiO_2 through a PECVD process and then we immerse it in heated benzoic acid and lithium benzoate to create single polarization waveguides. The waveguide is subsequently annealed to restore its acoustic properties. Finally, we pattern aluminum transducers onto the waveguides by conformal contact lithography employing a negative resist lift-off technique.

The goal of this work is to enable the inexpensive manufacturing of Scophony-architecture video displays [3] (both 2D and holographic video [4-5]) without the need for the horizontal scanning mirrors that typically limit the scalability of this technology.

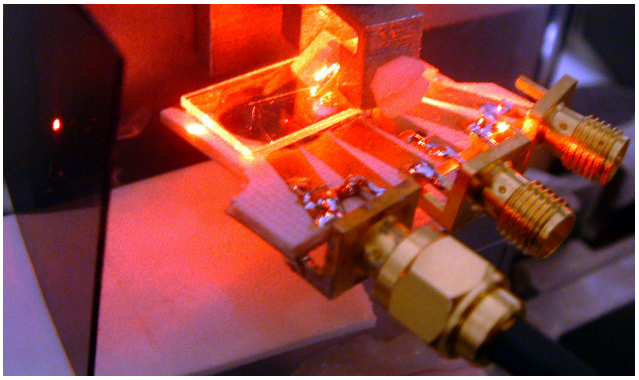

▲ Figure 1: A device undergoing testing.

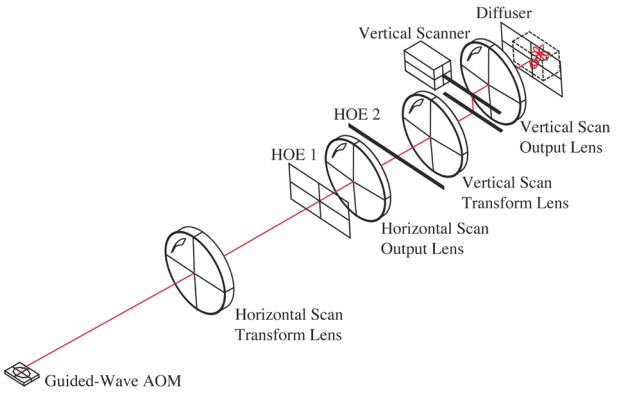

▲ Figure 2: Architecture of our display system.

REFERENCES

[1] C.S. Tsai, Q. Li, and C.L. Chang, "Guided-wave two-dimensional acousto-optic scanner using proton-exchanged lithium niobate waveguide," *Fiber and Integrated Optics*, vol. 17, pp. 57-166, July 1998.

[2] D. Smalley, "Integrated-optic holovideo," Master's thesis, Massachusetts Institute of Technology, Cambridge, MA, 2006.

[3] H.W. Lee, "The Scophony television receiver," *Nature*, vol. 142, pp. 59-62, July 1938.

[4] D.E. Smalley, Q.Y.J. Smithwick, and V.M. Bove, Jr., "Holographic video display based on guided-wave acousto-optic devices," *Proc. SPIE Practical Holography XXI*, vol. 6488, pp. 64880L:1-7, Jan. 2007.

[5] W. Plesniak, M. Halle, V.M. Bove, Jr., J. Barabas, and R. Pappu, "Reconfigurable image projection (RIP) holograms," *Optical Engineering*, vol. 45, no. 11, pp. 115801:1-15, Nov. 2006.

All Inorganic Colloidal Quantum-dot LEDs

V. Wood, J.M. Caruge, J.E. Halpert, M.G. Bawendi, V. Bulović
Sponsorship: NSF MRSEC, NSF NIRT, PECASE, ISN

LEDs with a quantum-dot (QD) emissive layer are an attractive technology for display and large-area lighting applications. QDs are nanoparticles that can be synthesized to emit anywhere from the ultraviolet to the infrared regions of the spectrum by changing their size and chemical composition. For example, varying the size of CdSe QDs from 17 to 120 Å tunes them to emit light at a wavelength between 470 nm to 630 nm [1]. Furthermore, QDs possess excellent color saturation and high photoluminescence efficiencies.

QDs have been successfully integrated into LEDs with organic charge transport layers. Such devices boast external quantum efficiencies (EQEs) ranging from of 0.4% for blue emission to 2.4% for red emission [2]. However, despite the high EQE and the ease of fabrication offered by organic semiconductor films, organic materials are susceptible to deterioration from atmospheric oxygen and water vapor. Device lifetimes can be improved with packaging, but this increases cost, making it difficult for QD-LEDs to compete with the already established technology of liquid crystal displays (LCDs). Furthermore, organic materials cannot sustain the high current density needed to realize an electrically pumped colloidal QD laser. In contrast, metal oxides are chemically and morphologically stable in air and can operate at high current densities.

We report the first all-inorganic QD-LEDs consisting of radio-frequency sputtered metal-oxide charge transport layers and a colloidal QD electroluminescent region. These devices manifest a 100-fold increase in EQE over the one previously reported inorganic QD structure [3]. Our device consists of ZnCdSe QDs sandwiched between resistive, p-type NiO and co-deposited ZnO and SnO_2 (see Figure 1). We measured a peak EQE of 0.09% at a current density of 3.2 A/cm² and a peak brightness of 1950 Cd/m² at a current density of 3.7 A/cm². As shown in Figure 2, light emission from the QDs is uniform across the device.

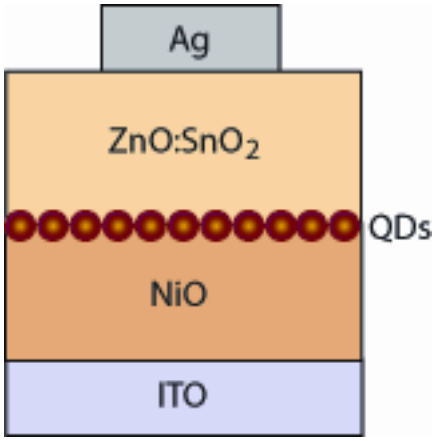

▲ Figure 1: Schematic of the all-inorganic QD-LED structure. Indium tin oxide (ITO) and Ag electrodes are used.

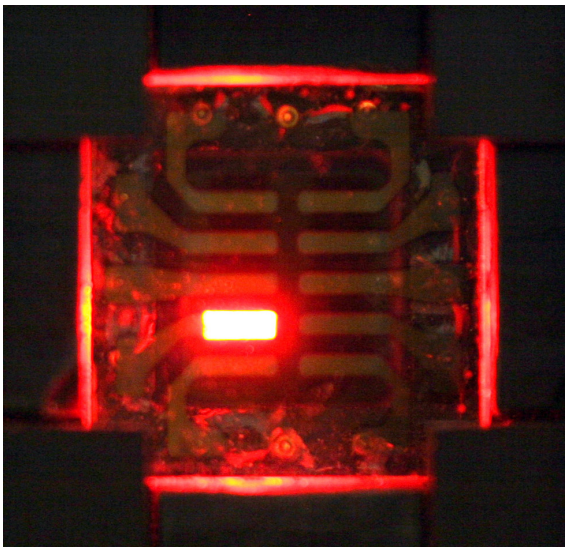

▲ Figure 2: All inorganic QD-LED operating under 6 V of applied bias and showing a brightness of 106 Cd/m².

REFERENCES

[1] C.B. Murray, D..J. Norris, and M.G. Bawendi. "Synthesis and characterization of nearly monodisperse CdE (E= S, Se, Te) semiconductor nanocrystallites," *Journal of the American Chemical Society*, vol. 115, pp. 8706-8715, Sep. 1993.

[2] P.O. Anikeeva, J.E. Halpert, M.G. Bawendi, and V. Bulović. "Electroluminescence from a red-green-blue colloidal quantum-dot monolayer," to be published.

[3] A.H. Mueller, M.A. Petruska, M. Achermann, D.J. Werder, E.A. Akhadov, D.D. Koleske, M.A. Hoffbauer, and V.I. Klimov. "Multicolor light-emitting diodes based on semiconductor nanocrystals encapsulated in GaN charge injection layers," *Nano Letters*, vol. 5, no. 6, pp. 1039-1044, June 2005.

Physics and Fabrication of J-aggregate Thin Films in Optical Microcavities for Nonlinear Optics Applications

M.S. Bradley, J.R. Tischler, Y. Shirasaki, V. Bulović
Sponsorship: DARPA, NDSEG, NSF MRSEC

Thin films of J-aggregates of cyanine dyes, which found wide use in the 20th century in the photographic film industry, exhibit narrow linewidth and large oscillator strength, enabling their use in the first room-temperature solid-state devices that exhibit the strong-coupling regime of Cavity Quantum Electrodynamics (Cavity QED) [1]. As we demonstrated in a recent study, layer-by-layer (LBL)-assembled J-aggregate thin films can be precisely deposited in a specific location in a microcavity and contain a high density of aggregates, contributing to the observation of a peak thin-film absorption coefficient of $1.05 \pm 0.1 \times 10^6$ cm^{-1}, among the highest ever measured for a neat thin film [2]. As LBL J-aggregate thin films are incorporated into more complex optoelectronic device structures, a more thorough understanding of the properties of exciton-polaritons in J-aggregate thin films is required to evaluate how the properties of the thin films change as deposition parameters are varied.

We investigate the optical and morphological properties of 5,6-dichloro-2-[3-[5,6-dichloro-1-ethyl-3-(3-sulfopropyl)-2(3H)-benzimidazolidene]-1-propenyl]-1-ethyl-3-(3-sulfopropyl) benzimidazolium hydroxide, inner salt, sodium salt (TDBC, anionic dye) J-aggregates, alternately adsorbed with poly-(diallyldimethylammonium chloride) (PDAC, cationic polyelectrolyte) on glass substrates. Figure 1 shows the reflectance spectra for substrates that underwent 8.5, 12.5, and 16.5 sequential immersions in cationic and anionic solution (SICAS) of PDAC/TDBC, where 0.5 SICAS refers to ending the growth on the PDAC immersion step. Figure 2 shows the reflectance spectra generated from T-matrix simulations using the dielectric function derived via quasi-Kramers-Kronig regression and multiples of the 8.5 SICAS film thickness. As the thickness of the film is increased, a photonic band gap develops similar to the "super-radiance" observed in multiple quantum-well structures and thin film organic crystals. The observation that the spectral broadening is due to a photonic band gap effect suggests that thicker LBL films may be used in cavity devices to boost Rabi splitting without sacrificing the linewidth of the cavity exciton-polariton.

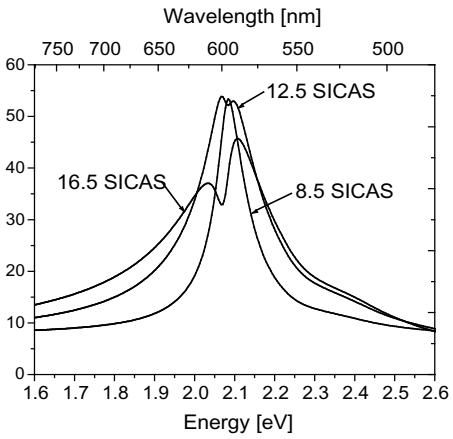

▲ Figure 1: Measured reflectance for samples with 8.5, 12.5, and 16.5 SICAS of PDAC/TDBC, where profilometry indicates film thicknesses of 16.3 ± 3.8 nm, 32.1 ± 6.6 nm, and 42.6 ± 5.3 nm, respectively.

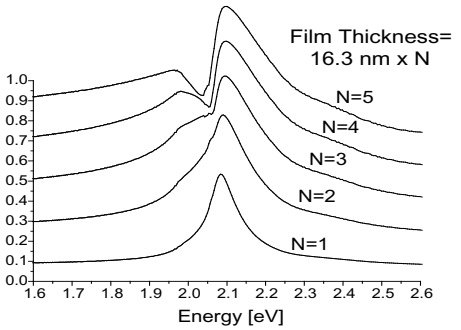

▲ Figure 2: Simulated reflectance using a dielectric function derived using a quasi-Kramers-Kronig regression with thickness multiples of 16.3 nm showing similar spectral broadening to that in Figure 1.

REFERENCES

[1] J.R. Tischler, M.S. Bradley, V. Bulović, J.H. Song, and A. Nurmikko, "Strong coupling in a microcavity LED," *Physical Review Letters*, vol. 95, no. 3, pp. 036401-036404, July 2005.

[2] M.S. Bradley, J.R. Tischler, and V. Bulović, "Layer-by-layer J-aggregate thin films with a peak absorption constant of 10^6 cm^{-1}," *Advanced Materials*, vol. 17, no. 15, pp. 1881-1886, Aug. 2005.

Organic Lateral Heterojunction Photoconductors

J. Ho, V. Bulović
Sponsorship: ISN

The purpose of this project is to develop solid-state, organic device structures capable of amplifying detection of chemical analytes and of efficiently transducting the chemosensitive response into an attenuated electrical signal. The main advantage to using organic materials in these structures is that they are synthetically flexible and can be tailored to respond to specific analytes. We demonstrated lateral heterostructures with in-plane electrodes consisting of an optically active, chemosensing layer and a charge-transport layer arranged as shown in Figure 1. In these structures, luminescence and corresponding exciton density in the chemosensitive layer are directly proportional to the density of the adsorbed analytes. It is advantageous to physically separate the sensing and transport functions in these chemical sensors as the separation allows us to optimize the transduction of chemosensitivity to the device current and to develop a reusable device platform for a variety of chemosensing applications.

In addition to developing a novel device platform for chemical sensing, we are also using this novel structure to study charge transport and exciton dynamics in organic thin films (Figure 1). Our devices consist of a series of gold interdigitated finger electrodes (W x L = 1500 μm x 4 μm) spaced 10 μm apart. The gold electrodes are photolithographically defined on glass before the organic layers are thermally evaporated. Lock-in measurements of the photocurrent spectra suggest external quantum efficiencies in the range of 10%. Initial experiments indicate an enhancement in photoresponse of the heterostructure devices over devices made from bulk films of both materials (Figure 2).

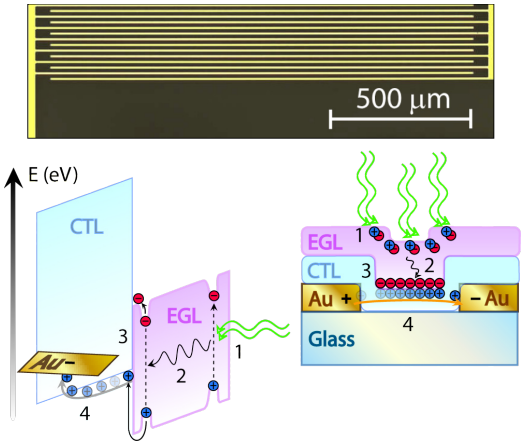

▲ Figure 1: The interdigitated gold fingers create 100 channels, each 1500 μm long by 10 μm wide, yielding an effective device area of approximately 1.5 mm². A digital image (a) of a set of device electrodes under magnification (50X). Energy band diagram (b) of a lateral bi-layer heterojunction photoconductor consisting of an exciton generation layer (EGL) and a charge transport layer (CTL). A cross-sectional view (c) of the same bi-layer device is also shown. Both illustrations depict the physical processes involved in steady-state device operation: (1) absorption, (2) exciton diffusion, (3) exciton dissociation and charge transfer, and (4) charge transport.

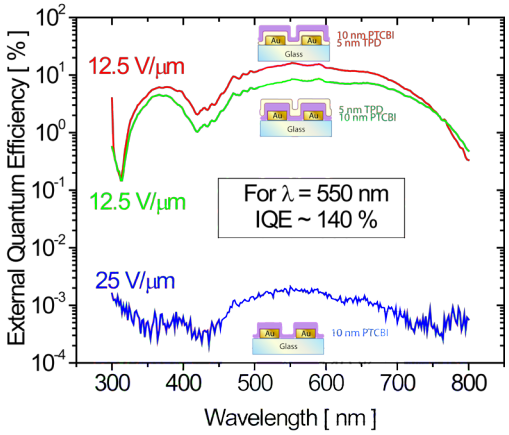

▲ Figure 2: Semi-logarithmic plot of external quantum efficiency (EQE) versus wavelength. Inset illustrations depict device structures and film thicknesses next to their corresponding curves, along with the electric fields applied. The Au/TPD device yields no measurable photoresponse and is not shown. Both heterojunction devices (red and green lines) yield orders of magnitude improvement in the (EQE) over the Au/PTCBI device (blue line) despite using lower bias voltages. At λ = 552 nm, the Au/PTCBI/TPD device (green) and Au/TPD/PTCBI device (red) yield EQEs of approximately 8% and 16%, respectively, which correspond to an internal quantum efficiency (IQE) of approximately 140%. This demonstrates that lateral bi-layer heterojunctions are capable of gain.

Colloidal Quantum-dot Memories

H. Abdu, J. Leu, K.K. Berggren, P. Anikeeva, O. Nayfeh, D.A. Antoniadis, M. Bawendi, V. Bulović
Sponsorship: SRC/FCRP MSD

Conventional non-volatile memories face obstacles to continued scaling, such as the inability to use thinner tunneling oxides and poor charge retention due to defects in the tunneling oxide. A possible solution is to replace the continuous floating gate, where charge is stored, with quantum dots (QDs). In the proposed structure, if a defect in the tunneling oxide exists in the oxide below a particular quantum dot, the rest of the quantum dots retain their charge due to poor lateral conduction between QDs. Because of this, quantum dot memories can achieve higher density, decreased power consumption, and improved performance.

We construct a QD capacitor, shown in Figure 1, by using 7nm CdZnS quantum dots as the floating gate. This monolayer of quantum dots was deposited using spin casting. Parylene was used as the gate dielectric because it can achieve good performance at low processing temperatures. This capacitor structure is a first step in achieving a QD memory cell, as it proves significant in understanding the quantum dot's ability to be written (charged), erased (discharged), and read (retain charge).

As shown in Figure 2, we demonstrate the functionality of the QD capacitor. The capacitance voltage (C-V) plot illustrates hysteresis, which indicates the flatband voltage shift that exists due to charge storage. Interestingly, in this device electrons and holes are stored at -5V and at +5V, respectively. Though having both types of charge being charged and discharged is acceptable, it provides insight to the dynamics of charge retention for each type.

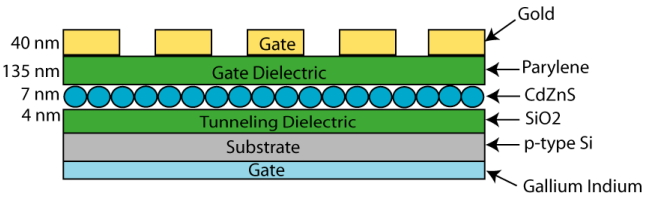

▲ Figure 1: Schematic diagram of a QD capacitor structure in which the CdZnS quantum dots have been used as the floating gate.

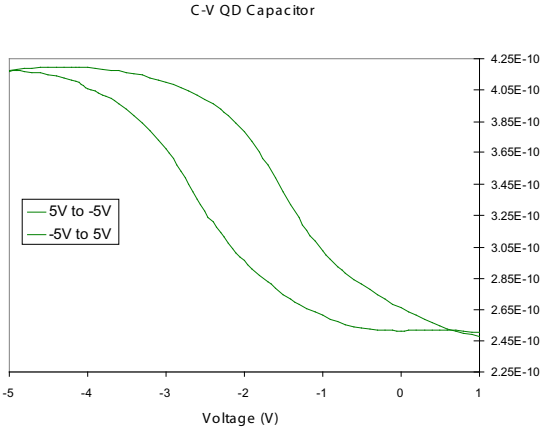

▲ Figure 2: A C-V plot of QD capacitor with characteristic hysteresis. Electron charging at -5V and hole charging at +5V.

REFERENCES

[1] K. Kinam, "Technology for sub-50nm DRAM and NAND flash manufacturing," *Proc. of the Electron Devices Meeting, IEDM Technical Digest*, Dec. 2005, pp. 323-326.

[2] W.L. Leong, P.S. Lee, S.G. Mhaisalkar, T.P. Chen, and A. Dodabalapur, "Charging phenomena in pentacene-gold nanoparticle memory device," *Applied Physics Letters*, vol. 90, pp. 042906, Jan. 2007.

[3] P. Pavan, R. Bez, P. Olivo, E. Zanoni, "Flash memory cells-an overview," *Proc. of the IEEE*, vol. 85, no. 8, pp. 1248-1271, Aug. 1997.

Recess Integration of Low-threshold VCSELs on Si CMOS ICs

J. Perkins, C.G. Fonstad
Sponsorship: SRC/FCRP IFC, NSF

Vertical Cavity Surface Emitting Lasers (VCSELs) integrated on silicon ICs have long been sought for optical interconnect applications to improve transfer rates in high-performance circuit applications. We have developed a new technique for micro-scale hybrid heterogeneous integration of optoelectronic devices on silicon integrated circuit wafers and have demonstrated it for optical interconnect applications using VCSELs. This technique allows for intimately connected devices to be integrated directly within the metal/dielectric stack covering a Si IC, allowing wafer scale monolithic processing of a multi-material, multi-technology integrated system.

Individual oxide-apertured 850-nm AlGaAs VCSEL device pills 8 μm tall and 90 μm in diameter have been bonded on contact pads at the bottom of recesses etched in the metal/dielectric stack covering a custom-designed, commercially processed silicon integrated circuit chip [1]. These devices are placed using a vacuum pick-up tool and solder-bonded in place. The VCSELs show threshold currents in the 1 to 10 mA range when driven by an on-chip Si transistor, and they display thermal characteristics superior to those of native substrate devices. These same devices can be used in more parallel assembly techniques, such as fluidic self-assembly [2] and magnetically assisted statistical assembly [3].

The superior heat-sinking of VCSELs integrated on Si in this manner is clear from the data shown in Figure 2 below: The thermal impedance of pills on their native (GaAs) substrate is 2.1 °C/mW. It increases to 4 °C/mW if the pill is etched loose of its substrate, but it falls to 2.6 °C/mW if bonded on a pad formed in metal layer 2 of a CMOS process. If it is bonded directly to the silicon substrate, the thermal impedance falls to under 2 °C/mW, the lowest value of all.

To summarize, low threshold VCSELs have been intimately integrated into the dielectric stack of a commercially produced Si IC. These devices showed continuous wave-lasing operation and no performance degradation over native substrate devices. The pseudo-monolithic integration technique demonstrated maintains the planarity of the IC surface and is performed entirely after the Si processing is completed. Devices made of many different materials can be integrated on full Si wafers using this technique, enabling unique hybrid optoelectronic integrated circuits.

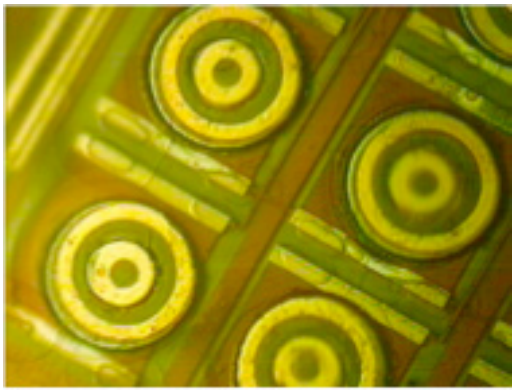

▲ Figure 1: A photomicrograph of four 90-μm-diameter VCSEL pills integrated in recesses on a CMOS IC chip. The next steps in the processing are to replanarize the surface, open contact vias, and deposit and pattern interconnect metal lines.

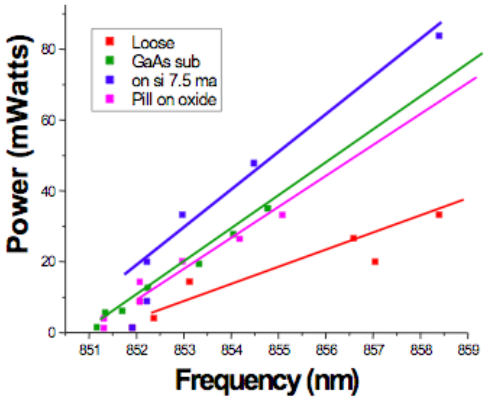

▲ Figure 2: The temperature-tuning of variously mounted VCSEL pills observed as the power dissipated in the pill increases. The loose pills (red) are the most poorly heat-sunk, and the pills bonded on Si (blue) are heat-sunk the best.

REFERENCES

[1] T. Simpkins, "Design, modeling, and simulation of a compact optoelectronic neural coprocessor," Ph. D. thesis, Massachusetts Institute of Technology, Cambridge, MA, 2005.

[2] J.K. Tu, J.J. Talghader, M.A. Hadley, and J.S. Smith, "Fluidic self-assembly of InGaAs vertical cavity surface emitting lasers onto silicon," *Electronics Letters*, vol. 31, pp. 1448, Aug. 1995.

[3] C.G. Fonstad. (January 2002) "Magnetically ssisted statistical assembly - a new heterogeneous integration technique," Singapore-MIT Alliance Symposium. [Online]. Available: http://hdl.handle.net/1721.1/3978

Micro-cleaved Laser Diode Platelets for Integration with Dielectric Waveguides on Silicon IC Wafers

J. Rumpler, C.G. Fonstad
Sponsorship: DARPA through ARL; Lincoln Laboratory IPI Program

The level of integration seen in commercial active photonic devices is at most a laser monolithically integrated with a modulator or a photodetector flip-chip bonded to an optical waveguide. To perform large scale optoelectronic integration, we have developed a technique that involves optimally fabricating building blocks, such as laser diodes or semiconductor optical amplifiers, and assembling these blocks in dielectric recesses on a system substrate, e.g., a silicon integrated circuit chip [1-2]. Our test case for demonstrating this technology is the integration of 1.55 μm InGaAsP edge-emitting laser diode blocks with planar silicon oxy-nitride waveguides on silicon. To this end, a process has been developed to fabricate freestanding edge-emitting laser platelets using a newly developed micro-cleaving technique. Micro-cleaving is used to simultaneously form highly reflecting end-facets and accurately control the length of the device to ± 1 μm.

The process begins with a device heterostructure that is a total of 5 microns thick and grown on an InGaAs etch-stop layer on an InP substrate. The top laser contact and the waveguide ridge are formed on the upper wafer surface, after which a pattern of long bars extending several laser lengths with notches locating the cleavage sites is etched through the heterostructure and the etch-stop layer. The wafer is embedded in polymer and mounted face down on a handle substrate. The original InP substrate is next removed, back contacts are deposited and patterned, and the polymer is finally removed, freeing the long thin bars from the handle substrate. The released bars are collected in a fluid medium and subjected to ultrasonic agitation, which causes them to cleave at the notches into individual laser platelets. Figure 1 shows a cleaved laser platelet; Figure 2 shows a close-up of the end facet and ridge waveguide. The slight bow in the laser platelet seen in Figure 1 is no longer present after the platelet has been bonded down.

The immediate objectives of the project are to complete characterization of these lasers, to develop an improved back-side metallization process, and to integrate platelet lasers with dielectric waveguides on silicon substrates.

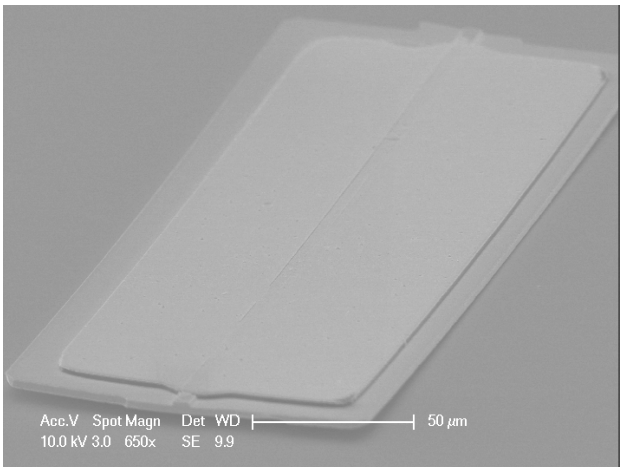

▲ Figure 1: A photomicrograph of an unbonded micro-cleaved edge-emitting ridge waveguide laser diode platelet.

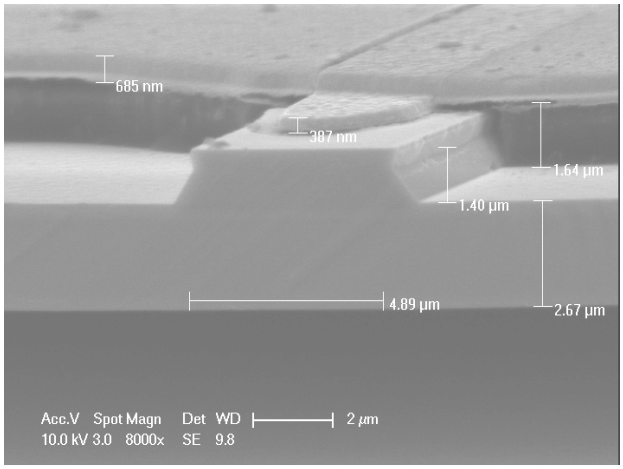

▲ Figure 2: A close-up view of the micro-cleaved end-facet of a laser diode platelet showing the ridge guide and top contact.

REFERENCES

[1] J. Rumpler, J.M. Perkins, and C.G. Fonstad, Jr., "Optoelectronic integration using statistical assembly and magnetic retention of heterostructure pills," in *Proc. of the Conference on Lasers and Electro-Optics (CLEO)*, vol. 2, pp. 16-21, May 2004.

[2] C.G. Fonstad, Jr., "Very large-scale monolithic heterogeneous integration: the epitaxy-on-electronics, Silicon-on-allium Arsenide, and aligned pillar bonding techniques," in *Heterogeneous Integration*, E. Towe, Ed., *Critical Reviews of Optical Engineering*, vol. CR76, Bellingham, WA: SPIE Optical Engineering Press, 2000.

Magnetically Assisted Statistical Assembly, Alignment, and Orientation of Micro-scale Components

D. Cheng, J. Perkins, J. Rumpler, C.G. Fonstad (in coll. with F. Cadieu, Queens College of CUNY, M. Zahn, MIT)
Sponsorship: Vitesse Chair

Fluidic assembly offers great promise for automated hybrid assembly of micro-scale components, but it has not yet lived up to its potential. This failure is largely because presently no good way exists to hold properly assembled components in place while simultaneously letting improperly positioned components disassemble and reassemble until they are properly positioned. We are researching the use of magnetic attraction to provide a "glue" to hold properly assembled components in place, eliminate their disassembly, and allow the assembly to go to completion across a wafer [1]. We are also investigating the use of patterned magnetic films to accurately orient, align, and position assembled components.

We call our assembly process magnetically assisted stochastic assembly (MASA). The two unique elements of MASA not present in conventional fluidic assembly are a soft magnetic film on the bottom surface of the component to be integrated and a patterned hard magnetic film on the bottom of the recess in which it is to be located (i.e., assembled). The attraction between these two films holds a component in place in its recess and prevents disassembly. In the basic embodiment of MASA, the soft magnetic film uniformly covers the bottom surface of the component. The hard magnetic film in the recesses is permanently magnetized and is patterned to control the strength and extent of the attracting field experienced by the soft magnetic film on the components. By suitably designing the pattern, calculations indicate that it is possible to tailor the magnetic fields and to create a situation in which the component feels no attraction when it is outside a recess, or is upside down in a recess, and is attracted only toward the hard magnetic film when it is entering a recess in the proper orientation. In second-generation MASA, both the hard and the soft magnetic films will be patterned so that the attractive force will also rotationally orient and laterally position the component in place within the recess.

Our efforts have been hampered for several years by the lack of a good source of hard magnetic thin films, but this situation has changed significantly recently as we have established a collaboration with Professor Fred Cadieu at Queens College of CUNY, an expert in the sputter deposition of Sm-Co films. He has supplied us with several films and we have already developed a wet etch which allows us to pattern these films and remove them from the side-walls of recesses. We presently seek funding for a research program in this area.

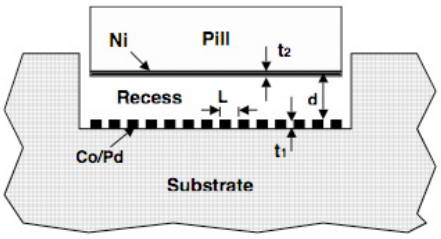

▲ Figure 1: A cross-sectional cartoon illustrating the application of magnetically assisted assembly to recess integration. The variables indicated in the drawing correspond to the model used to calculated the magnetic force intensity in Figure 2.

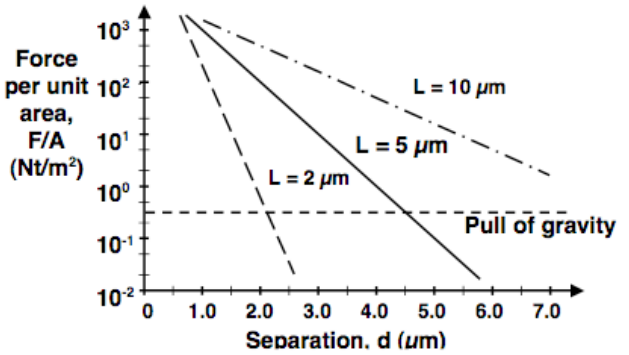

▲ Figure 2: The attractive force per unit area as a function of the separation between the pill and the bottom of the recess. The hard magnetic film is 500 nm thick and the Ni film is 200 nm. The pull of gravity on a 6-μm-thick GaAs pill is also indicated.

REFERENCES

[1] J. Rumpler, J.M. Perkins, and C.G. Fonstad, Jr., "Optoelectronic integration using statistical assembly and magnetic retention of heterostructure pills," in *Proc. of the Conference on Lasers and Electro-Optics (CLEO)*, May 2004, vol. 2, pp. 16-21.

Co-axial Integration of III-V Ridge-waveguide Gain Elements with SiO_xN_y Waveguides on Silicon

E. Barkley, J. Rumpler, J. Perkins, C.G. Fonstad
Sponsorship: DARPA through ARL

Significant progress has been made fabricating photonic integrated circuits on Si and integrating them with CMOS ICs, but the need for compatible optical gain elements (laser sources and optical amplifiers) still remains. Recently researchers at UCSB and Intel have had good success integrating III-V gain elements with Si-based dielectric waveguides using evanescent coupling [1]. At MIT, we have developed an alternate approach that uses co-axial coupling of III-V ridge waveguide devices and Si-based dielectric waveguides. This integration process includes first fabricating micro-scale device platelets, such as laser diodes (LDs) or optical amplifiers (SOAs), from commercially grown heterostructures, and then assembling these platelets in dielectric recesses etched through silicon oxy-nitride/silicon dioxide waveguides on Si wafers (ultimately this step will be done on IC wafers).

The essential ingredients for efficient coupling between the ridge waveguide devices and the dielectric waveguides are (1) matching the mode profiles, (2) accurately aligning the waveguides laterally and vertically, and (3) minimizing the separation between the guide segments. Standard dry-etch processes can be used to keep the space between the recess wall and the side of the laser small; the vertical offset between the core of the dielectric waveguide and the active region of the in-plane laser is kept small by monitoring layer thicknesses during epitaxy and deposition. To keep the gap between the guide ends small while also having a good cavity end facets, we use precision micro-cleaving; this enables us to control the cavity length to within 1 micron.

Measurements on integrated assemblies with air filling the gap between the guides indicate that coupling losses as low as 5 dB are obtained when the guides are well aligned and the gap is less than 1 micron [2]. Other measurements and computer simulations indicate that using a gap fill with n = 2.2 (e.g., silicon nitride) and improving tailoring of the vertical mode profile in the III-V guide can reduce this loss to below 1 dB. Other work in progress in this program includes integrating angle-mounted SOAs with dielectric waveguides and developing a new laser design using a silicon oxy-nitride waveguide DFB structure and a high-index gap fill.

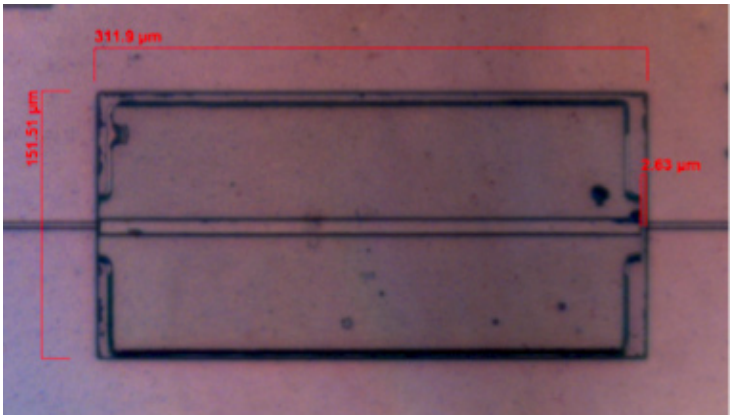

▲ Figure 1: A photomicrograph showing a top view of a III-V ridge waveguide platelet positioned in a dielectric recess and aligned with a silicon oxy-nitride waveguide. Transmission measurements through passive waveguide assemblies were used to characterize the coupling losses between the two types of guide.

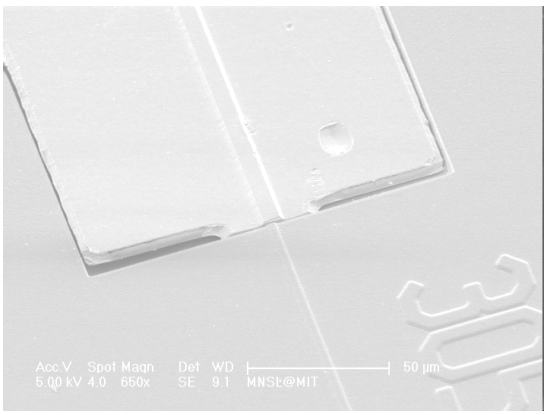

▲ Figure 2: A close-up photomicrograph showing the alignment between an InGaAsP/InP ridge waveguide platelet and a buried silicon oxy-nitride waveguide. Coupling losses as low as 3 dB were measured.

REFERENCES

[1] A.W. Fang, H. Park, O. Cohen, R. Jones, M.J. Paniccia, and J.E. Bowers, "Electrically pumped hybrid AlGaInAs-silicon evanescent laser," *Optics Express*, vol. 14, pp. 9203-9210, Oct. 2006.

[2] E.R. Barkley, "The integration of InP/InGaAsP ridge waveguide structures with dielectric waveguides on silicon," Ph.D. thesis, Massachusetts Institute of Technology, Cambridge, MA, 2006.

Electrical Characteristics of Ge-on-Si LPCVD-grown Photodiodes

N. DiLello, O.O. Olubuyide, H. Buss, J.L. Hoyt
Sponsorship: DARPA, SRC Student Fellowship

Germanium is a promising candidate for use in CMOS-compatible photodiodes. Its strong absorption in the 1.55-μm range and relative ease of integration on silicon substrates make it suitable for telecommunications systems as well as in other high-speed electronic photonic integrated circuits. An important figure of merit in these photodiodes is the reverse leakage current. o reduce power consumption and improve signal-to-noise ratio, it is important that the diodes have a low leakage current in reverse bias, typically measured at -1 V. This study has investigated the leakage current of germanium photodiodes grown by low-pressure chemical vapor deposition (LPCVD) using an Applied Materials Epitaxial Reactor.

In the diodes that were fabricated and measured, we observed that some had leakage currents that were area-dependent (AD) and some were perimeter-dependent (PD). Figure 1 shows I vs. V curves for area-dominated diodes of various sizes while Figure 2 has the data for PD diodes. Previous measurements of these diodes resulted in an area dependence of $J_A = 8.5$ mA/cm^2 for the AD diodes and $J_A = 2.4$ mA/cm^2 for the PD diodes [1]. Furthermore, these measurements also resulted in a perimeter dependence of $J_P = 50$ nA/cm for the AD diodes and $J_P = 0.06$ mA/cm for the PD diodes [1]. These numbers are quoted at a reverse bias of -1 V. The AD diodes thus have a much lower perimeter leakage current, indicating that the passivation of trap states near the dielectric/Ge interface is much better on the AD diode wafer, compared to the PD diodes. These results motivate further work on materials and processing parameters that improve Ge surface passivation and reduce perimeter leakage currents.

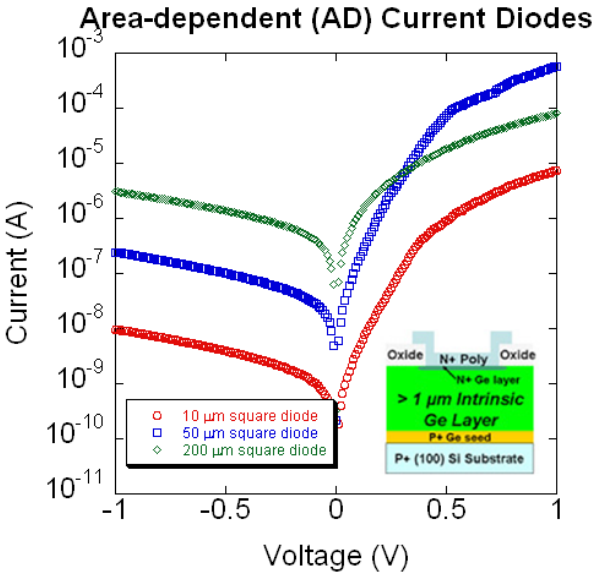

▲ Figure 1: The I vs. V curves for various sizes of square diodes. The leakage current at -1 V scales with the area of the devices. The inset is a cross-sectional view of the Ge-on-Si p-i-n photodiode.

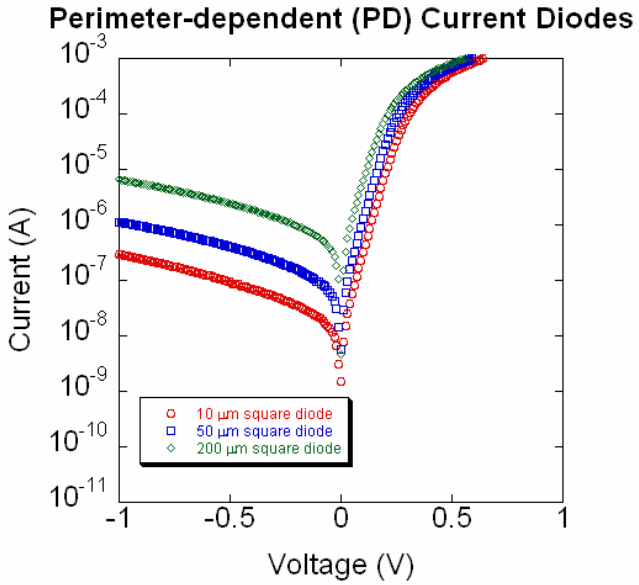

▲ Figure 2: The I vs. V curves for various sizes of square diodes. The leakage current at -1 V scales with the perimeter of the devices.

REFERENCES

[1] O.O. Olubuyide, "Low-pressure epitaxial growth, fabrication and characterization of Ge-on-Si photodiodes," Ph.D. thesis, Massachusetts Institute of Technology, Cambridge, MA, 2007.

Development of Terahertz Quantum-cascade Lasers

B. Williams, S. Kumar, A. Lee, Q. Qin, Q. Hu (in coll. with J. Reno, Sandia National Lab)
Sponsorship: NSF, NASA, AFOSR

The terahertz frequency range (1-10 THz) has long remained undeveloped, mainly due to the lack of compact, coherent radiation sources. Transitions between sub-bands in semiconductor quantum wells were suggested as a method to generate long wavelength radiation at customizable frequencies. However, because of difficulties in achieving population inversion between narrowly separated sub-bands and mode confinement at long wavelengths, THz lasers based on intersub-band transitions were developed only very recently. We have developed THz quantum-cascade lasers based on resonant-phonon-assisted depopulation and using metal-metal waveguides for mode confinement. The top-left of Figure 2 illustrates schematics of both features are illustrated in the top-left figure. Based on the combination of these two unique features, we have developed many THz QCLs with record performance measurements, including a maximum pulsed operating temperature at ~170 K (top-right), a maximum power of ~250 mW (bottom-right), and the longest wavelength (~190 μm) QCL to date without the assistance of magnetic fields (bottom-left).

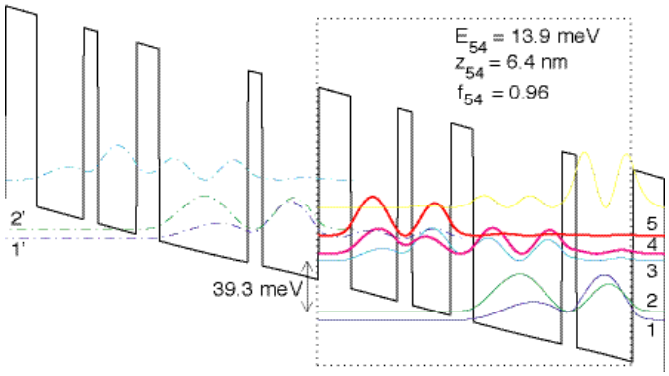

▲ Figure 1

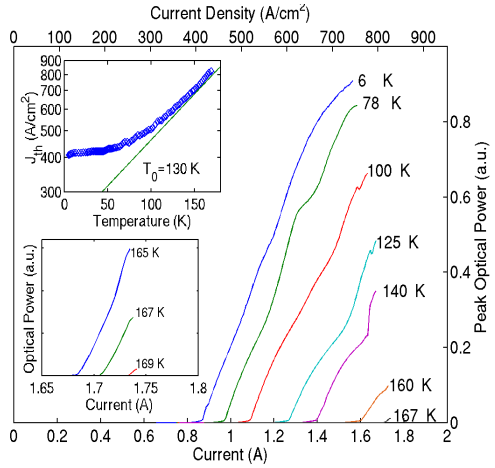

▲ Figure 2

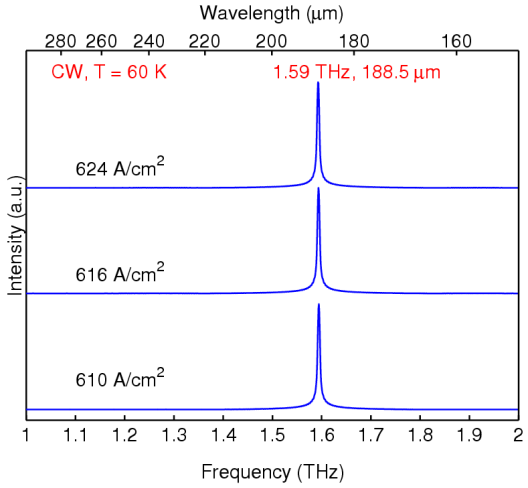

▲ Figure 3

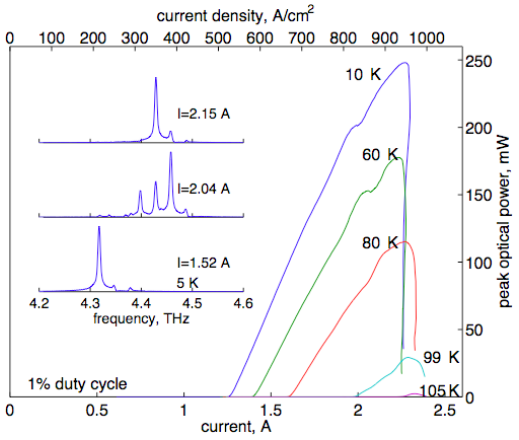

▲ Figure 4

Waveguide-integrated Ge p-i-n Photodetectors on a Si Platform

D. Ahn, J. Liu, C. Hong, M. Beals, J. Michel, L.C. Kimerling
Sponsorship: DARPA EPIC Program

The combined integration of electronic and photonic circuits has become an increasingly promising technology for the high functionality extension of traditional technology shrink. For an electronic-photonic integrated circuit (EPIC) on-chip, an essential component is the waveguide-integrated photodetector on a Si CMOS platform to convert optical signals to electrical ones. We demonstrate high performance Ge p-i-n photodetectors integrated with waveguides on a Si platform with two coupling schemes: vertical coupling and butt-coupling. In the vertical coupling scheme, the light couples evanescently from the waveguide to the Ge detector below it, while in the butt-coupling scheme, the output end of the waveguide directly inputs to the Ge photodetector. With the vertical coupling scheme, a high responsivity of ~1.0 A/W in the wavelength rage of 1470-1570 nm and a 3dB bandwidth of ~7.2 GHz have been demonstrated. With the butt-coupling scheme we have achieved a high responsivity of 1.0 A/W at 1520 nm and a 3dB bandwidth greater than 4.5 GHz. The devices were fabricated completely with a CMOS process, and they can be integrated with CMOS circuitry to achieve electronic and photonic integration on Si.

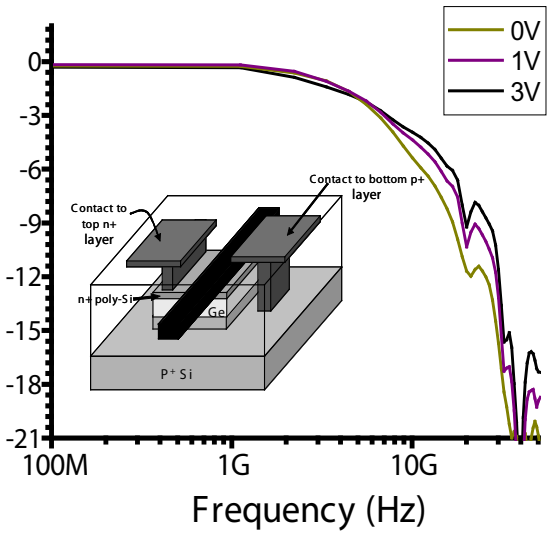

▲ Figure 1: Frequency response at different reverse biases of a Ge p-i-n photodetector on Si vertically coupled to a silicon nitride waveguide. The inset of the figure schematically shows the structure of the device.

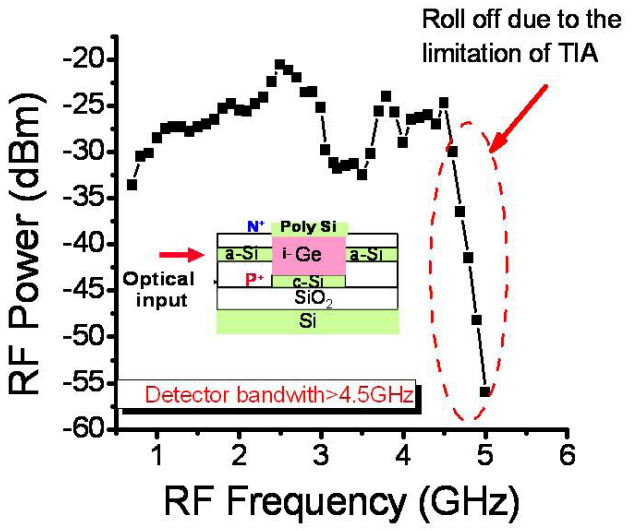

▲ Figure 2: Frequency response at 3V reverse bias of a Ge p-i-n photodetector on Si butt-coupled to a silicon waveguide. The inset of the figure schematically shows the structure of the device.

REFERENCES

[1] J.Liu, D. Pan, S. Jongthammanurak, K. Wada, L.C. Kimerling, J. Michel, J. Chen and F.X. Kärtner, "Design of monolithically integrated GeSi electroabsorption modulators and photodetectors on an SOI platform," *Optics Express*, vol. 15, pp. 623-628, Jan. 2007.

[2] D. Ahn, C. Hong, J. Liu, W. Giziewicz, M. Beals, L.C. Kimerling, and J. Michel, "High-performance, waveguide-integrated Ge photodetectors," *Optics Express*, vol. 15, no. 7, pp. 3916-3921, Apr. 2007.

[3] J.F. Liu, D. Ahn, C.Y. Hong, D. Pan, S. Jongthammanurak, M. Beals, L.C. Kimerling, J. Michel, A.T. Pomerene, D. Carothers, C. Hill, M. Jaso, K.Y. Tu, Y.K. Chen, S. Patel, M. Rasras, A. White, and D.M. Gill, "Waveguide integrated Ge p-i-n photodetectors on a silicon-on-insulator platform," *Optics Valley of China International Symposium on Optoelectronics*, Nov. 2006, pp. 1-4.

High-efficiency Si Thin-film Solar Cells with Textured Photonic Crystal Backside Reflector

L. Zeng, P. Bermel, Y. Yi, N. Feng, B.A. Alamariu, J. Liu, C. Hong, X. Duan, J.D. Joannopoulos, L.C. Kimerling
Sponsorship: National Renewable Energy Laboratory

Thin-film solar cells (TFSC) are the leading candidates for next generation photovoltaic applications. Currently, the efficiency of TFSC, however, is very low due to its weak absorption of long wavelength photons. To tackle this problem, we invented a new light-trapping scheme using textured photonic crystal as a backside reflector with a reflectivity as high as 99.8%, which can enormously elongate the optical path length for complete light absorption. It is composed of a reflection grating and a distributed Bragg reflector (DBR) [1]. In this work, optimization of the back reflector is systematically designed and conducted through both simulation and experiments.

The scattering matrix method is used to simulate the efficiency enhancement of solar cells with different back reflector parameters. Specifically, as for the gratings, both 1D and 2D submicron gratings are developed. Regarding 1D gratings, period and etch depth, as well as the duty cycle, are studied in detail and the best combination is realized. In the case of 2D gratings, the influence of variations in two perpendicular directions is explored. As for DBR, SiO_2/Si materials are used, and the period is optimized to make the stopband as wide as required by different solar cell thickness. The highest power conversion efficiency is achieved for a given solar cell thickness with an optimized back reflector structure. Figure 1 shows the significant absorption enhancement in a 5-μm-thick solar cell due to the back reflector. As an example of parameter optimization, Figure 2 depicts grating etch-depth optimization in a 5-μm-thick solar cell, with cell efficiency as the optimization criterion. Furthermore, trends of the variation of optimal back reflector parameters and anti-reflection coating thickness with solar cell thicknesses are identified.

Experimentally, silicon-on-insulator solar cells are fabricated with optimal back reflector parameters to verify the design and avoid complication-of-materials issues. The optimized back reflector design can be readily applied to monocrystalline and polycrystalline Si thin-film solar cells.

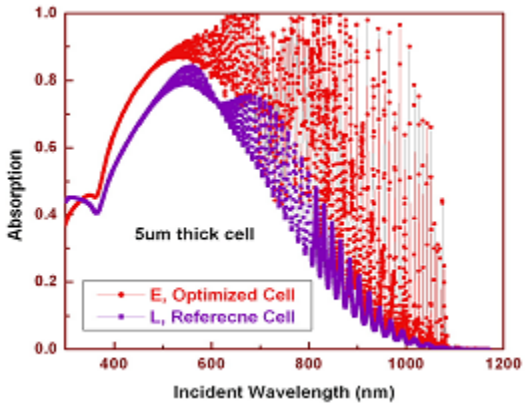

▲ Figure 1: Significantly enhanced absorption of a 5-μm-thick Si solar cell due to the back reflector.

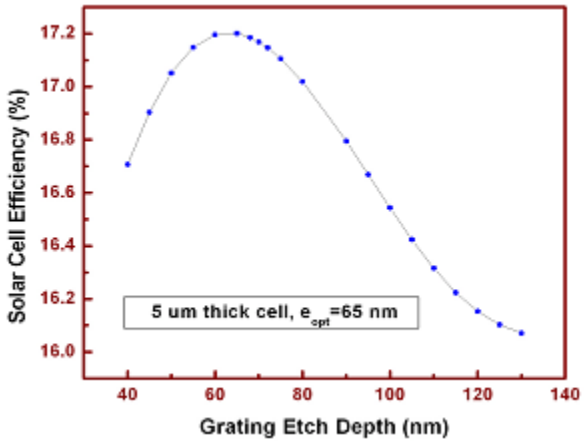

▲ Figure 2: Grating etch-depth optimization for a 5-μm-thick Si solar cell to achieve the highest efficiency.

REFERENCES

[1] L. Zeng, Y. Yi, C. Hong, J. Liu, N. Feng, X. Duan, B.A. Alamariu, and L.C. Kimerling, "Efficiency enhancement in Si solar cells by textured photonic crystal back reflector," *Applied Physics Letters*, vol. 89, pp. 111111-111114, Sept. 2006.

Large Electro-optic Effect in Tensile Strained Ge-on-Si Films

S. Jongthammanurak, J. Liu, K. Wada, D.D. Cannon , D.T. Danielson, D. Pan, L.C. Kimerling, J. Michel
Sponsorship: DARPA EPIC Program

Silicon-based integrated photonic circuits represent a promising technology for high-capacity data communication and high-speed parallel-signal processing [1]. Optical modulators are a key component in these integrated circuits for encoding information on optical carriers. Existing silicon modulators use the plasma dispersion effect to modulate refractive index. The bandwidth limit of these devices is ~1-10GHz [2-3] and is determined by the slower rate of either the injected carrier sweep-out or electron-hole recombination process. While this device represents a new paradigm for electro-optic silicon-based components, its footprint and power dissipation do not scale to levels of high density integration. This report is the first of a study of electric-field modulation of refractive index in silicon-based materials for high-speed applications. We find that germanium integrated monolithically on silicon exhibits a large, field-modulated electro-optic effect in the weakly absorbing regime.

The field-dependence of absorption in the Ge films was measured from spectral responsivity measurements of Ge-on-Si p-i-n diodes. The experimental data were analyzed using the generalized Franz-Keldysh formalism and independently measured valence band edge shifts of the light- and heavy-hole energy positions in response to biaxial stress, using Photoreflectance technique. An electric field of 70kV/cm increased the absorption coefficient from 62 cm^{-1} to 230 cm^{-1} at 1647 nm, in very good agreement with the theory (Figure 1). At 1647 nm, the electro-optic coefficient $\Delta n/F$ for the strained Ge film is 280 pm/V, as compared to 160 pm/V for unstrained Ge. The measured $\Delta\alpha/\alpha$ ratios for the strained and unstrained Ge films are 3.03 and 1.11, respectively (Figure 2). These results show that the Ge-on-Si epitaxial films have significant potential for efficient CMOS-compatible, field-induced, optical modulator devices.

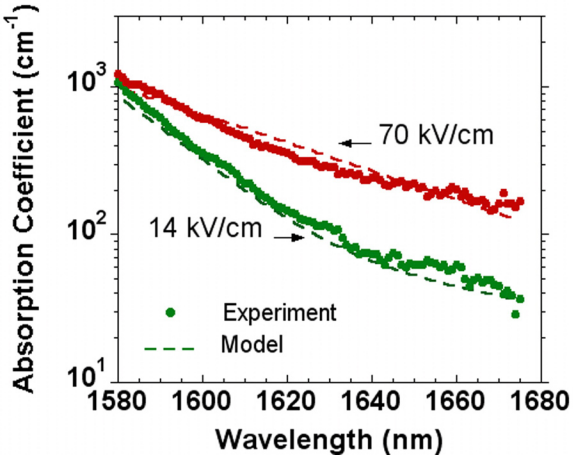

▲ Figure 1: Excellent fit of experimental data to the model based on the generalized Franz-Keldysh formalism without fitting parameters.

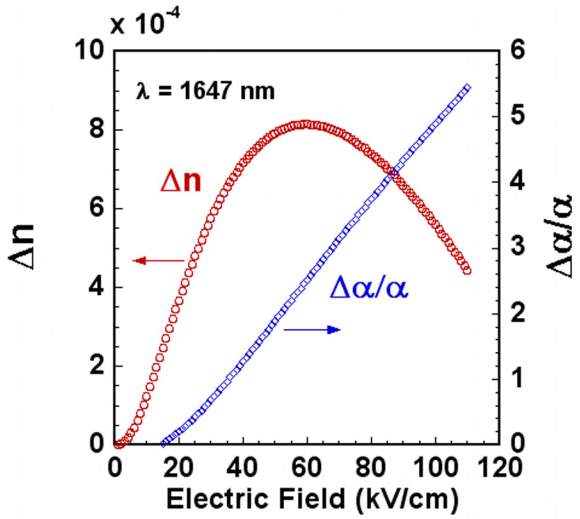

▲ Figure 2: Application of the model to predict Δn and $\Delta\alpha/\alpha$ at 1647- nm wavelength *as* a function of the applied electric field.

REFERENCES

[1] R.A. Soref, "Silicon-based optoelectronics," *Proceedings of the IEEE*, vol. 81, no. 12, pp. 1687-1706, Dec. 1993.

[2] A. Liu, R. Jones, L. Liao, D. Samara-Rubio, D. Rubin, O. Cohen, R. Nicolaescu, and M. Paniccia, "A high-speed silicon optical modulator based on a metal–oxide–semiconductor capacitor," *Nature*, vol. 427, pp. 615-618, Feb. 2004.

[3] Q. Xu, B. Schmidt, S. Pradhan and M. Lipson, "Micrometre-scale silicon electro-optic modulator," *Nature*, vol. 435, pp. 325-327, May 2005.

Low-loss Integrated Planar Chalcogenide Waveguides for Microfluidic Chemical Sensing

J. Hu, V. Tarasov, N. Carlie, L. Petit, A. Agarwal, K. Richardson, L.C. Kimerling
Sponsorship: DOE

We have fabricated and tested, to the best of our knowledge, the first microfluidic device monolithically integrated with planar chalcogenide glass waveguides on a silicon substrate. High-quality $Ge_{23}Sb_7S_{70}$ glass films have been deposited onto oxide-coated silicon wafers using thermal evaporation, and high-index-contrast channel waveguides have been defined using SF_6 plasma etching. Microfluidic channel patterning in photocurable resin (SU8) and channel sealing by a polydimethylsiloxane (PDMS) cover completed the device fabrication. The chalcogenide waveguides yield a transmission loss of 2.3 dB/cm at 1550 nm.

Sensor performance was tested by monitoring the optical output while injecting a solution of N-methylaniline mixed with a solution of carbon tetrachloride into the microfluidic channel. The N-H bond in N-methylaniline is known to exhibit an absorption peak near 1500 nm, which was used as the characteristic fingerprint for chemical identification in our test. The resultant absorption spectrum exhibits a well-defined absorption peak at 1496 nm, which is in excellent agreement with a traditional absorption measurement carried out on a Cary 5E UV-Vis-NIR dual-beam spectrophotometer. Since carbon tetrachloride is transparent in the wavelength range investigated, this spectral peak is unambiguously assigned to N-H bond vibrational absorption. The peak absorption in dB at 1496 nm was measured for different concentrations of N-methylaniline solution in carbon tetrachloride and the result is shown in Figure 2. The excellent linear fit suggests that the sensor exhibits linear response when varying analyte concentrations. From our experiments, a sensitivity of this sensor down to a N-methylaniline concentration 0.7 vol. % is expected. Given the low-cost fabrication process used and robust device configuration, our integration scheme provides a promising device platform for chemical sensing applications.

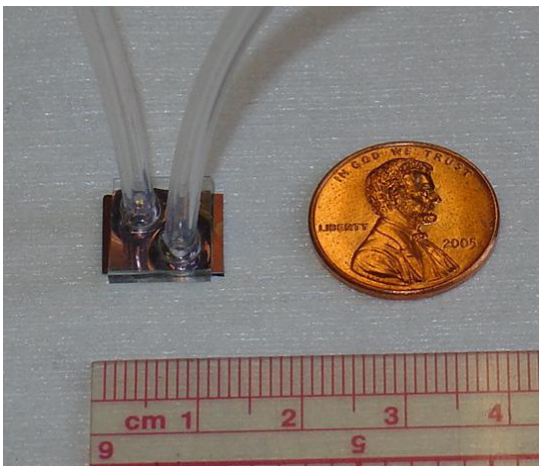

▲ Figure 1: Photo of the assembled microfluidic chip with fluid inlet and outlet tubing; The channels and $Ge_{23}Sb_7S_{70}$ waveguides are too small to resolve in the image.

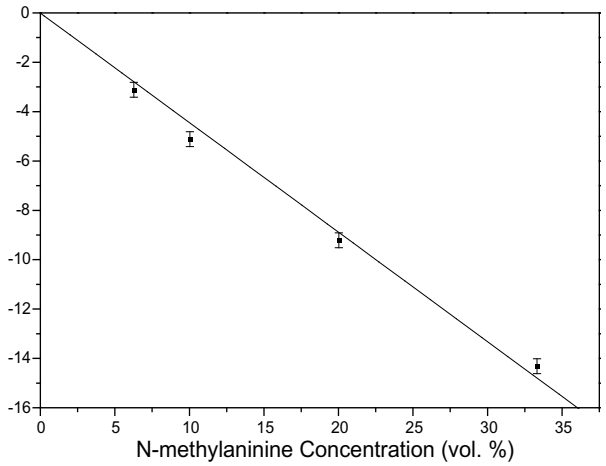

▲ Figure 2: Peak absorption of N-methylaniline solution in carbon tetrachloride at 1496-nm wavelength measured using the waveguide evanescent sensor as a function of N-methylaniline volume concentration, indicating good linearity of the sensor response.

REFERENCES

[1] J. Hu, V. Tarasov, N. Carlie, L. Petit, A. Agarwal, K. Richardson, and L. Kimerling, "Fabrication and testing of planar chalcogenide waveguide integrated microfluidic sensor," *Optics Express*, vol. 15, pp. 2307-2314, Mar. 2007.

[2] J. Hu, V. Tarasov, N. Carlie, R. Sun, L. Petit, A. Agarwal, K. Richardson, and L. Kimerling, "Low-loss integrated planar chalcogenide waveguides for microfluidic chemical sensing," *Proc. SPIE*, vol. 6444, pp. 64440N:1-4, Feb. 2007.

Multispectral One-dimensional Photonic Crystal Photodetector

X.C. Sun, J.J. Hu, C.Y. Hong, J.F. Viens, XM. Duan, R. Das, A.M. Agarwal, L.C. Kimerling
Sponsorship: Deshpande Center for Technological Innovation, Lincoln Laboratory

Applications such as multi-chemical detection, biological sensing, multispectral imaging and spectroscopy call for specialized photodetectors that are capable of selectively sensing specific wavelengths simultaneously, namely multispectral photodetection [1-3]. Here we present a designed and fabricated photonic crystal structure incorporating photoconductive layers to achieve simultaneous multispectral detection [4]. This novel photoconductor pixel exploits resonant cavity enhancement (RCE) for multispectral capability, high quantum efficiency, and dramatically suppressed shot noise. In a quarter-wavelength stack (1-D photonic crystal), standing wave patterns (defect modes) form at resonant wavelengths when defect layers are present. If the thicknesses and positions of photoconductive layers are optimally tuned with respect to the modal overlap with the defect modes, each photoconductive layer will selectively absorb only one specific resonant wavelength. Besides multispectral capability, the proposed design features enhanced optical absorption due to the cavity enhancement effect and allows the use of thinner photoconductive layers, which significantly reduces shot noise and improves the performance of photoconductive detectors.

The fabricated device exploits mode discrimination and resonant cavity enhancement to provide simultaneous multispectral detection capability, high quantum efficiency, and dramatically suppressed shot noise. The use of amorphous Si as active material reduces fabrication cost and simplifies device processing by eliminating the complicated single-crystal growth process. Detectivities as high as 2.6×10^{10} cmHz$^{1/2}$W^{-1} and 2.0×10^{10} cmHz$^{1/2}$W^{-1} at the two pre-selected wavelengths, 632nm and 728nm, respectively, were achieved.

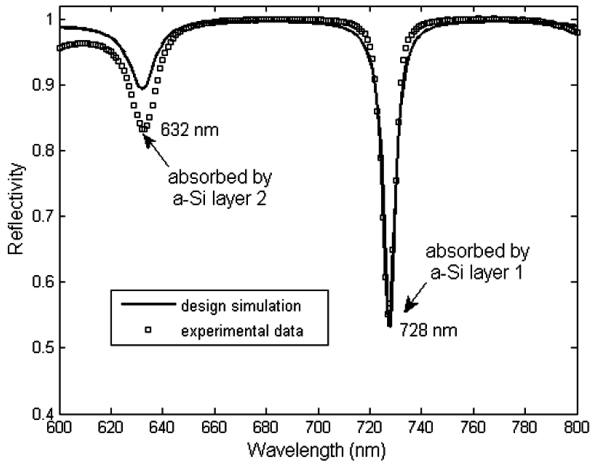

▲ Figure 1: Experimental data and transfer matrix simulation result of the photonic crystal stack reflectivity showing two resonant absorption peaks at 632 nm and 728 nm, which are selectively absorbed by the first two of the three amorphous Si layers, respectively.

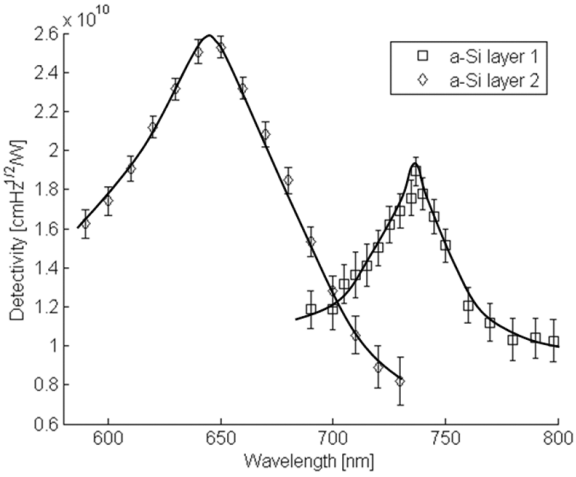

▲ Figure 2: Detectivity spectra at 10V of the first two amorphous Si photoconductive layers showing wavelength selectivity. Detectivities are calculated from data measured using a tungsten halogen lamp monochromator.

REFERENCES

[1] S. Baronti, A. Casini, F. Lotti, and S.Porcinai, "Multispectral imaging system for the mapping of pigments in works of art by use of principal-component analysis," *Applied Optics*, vol. 37, pp. 1299-1309, Mar. 1998.

[2] S.W. Seo, D.L. Geddis, and N.M. Jokerst, "3-D stacked thin-film photodetectors for multispectral detection applications," *IEEE Photonics Tech. Lett.*, vol. 15, p. 578, Apr. 2003.

[3] D. Krapf, B. Adoram, J. Shappir, A. Saar, S.G. Thomas, J.L. Liu, and K.L. Wang, "Infrared multispectral detection using Si/SixGe1–x quantum well infrared photodetectors," *Applied Physics Letters*, vol. 78, pp. 495-497, Jan. 2001.

[4] X.C. Sun, J.J. Hu, C.Y. Hong, J.F. Viens, X.M. Duan, R. Das, A.M. Agarwal, and L.C. Kimerling, "Multispectral pixel performance using a one-dimensional photonic crystal design," *Applied Physics Letters*, vol. 89, pp. 223522:1-3, Nov. 2006.

Super-collimation of Light in Photonic Crystal Slabs

T. Shih, A. Kurs, M. Dahlem, K. Hall, M. Kesler, G.S. Petrich, M. Soljacic, J.D. Joannopoulos, E.P. Ippen, L.A. Kolodziejski
Sponsorship: NSF MRSEC, SRC/FCRP IFC, STTR

A super-collimator is a device in which light is guided by the dispersion properties of a photonic crystal slab rather than by defects or by traditional index guiding. Photonic crystals (PhC) form the essence of the super-collimation effect. The successful fabrication and testing of a super-collimator consisting of a two-dimensional PhC that is composed of a square lattice of cylindrical holes etched into silicon have been performed. Super-collimation for more than 600 isotropic diffraction lengths has been observed for this device (the isotropic diffraction length is the length over which the light beam spreads by square root of 2).

The current goal of the research is to demonstrate super-collimation with a two-dimensional PhC that is composed of a square lattice of cylindrical silicon posts, rather than holes. A super-collimator that is composed of posts allows fluids to more easily fill and flow through the spaces between the posts, making this design more suitable for applications such as chemical sensing. Two fabrication processes have been developed and tested. The device has been fabricated using a silicon-on-insulator wafer in which the low-index silicon dioxide layer (3 μm thick) is used to minimize radiation loss into the high-index silicon substrate. The photonic crystal occupies the entire surface of the super-collimator so that the cleaved edges of the photonic crystal function as input or output facets of the device. The initial design with the help of the Ab Initio Physics Group has focused on realizing super-collimation at a wavelength of 1530 nm so that the lattice constant, post radius, and Si thickness were 437.5 nm, 250 nm, and 700 nm, respectively. Figure 1 is a scanning electron microscope image of the finished device. Testing in collaboration with the Optics and Quantum Electronics Group is in progress.

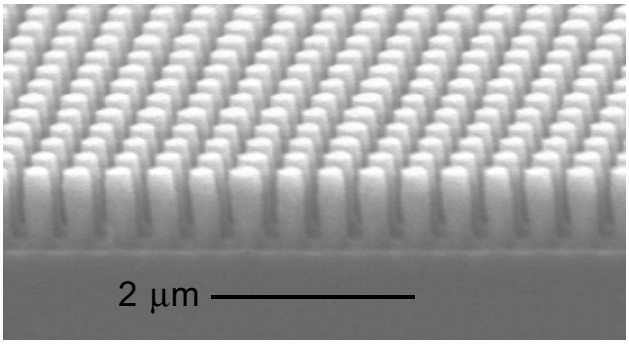

▲ Figure 1: An SEM image of the super-collimator. The silicon posts are 700 nm tall and rest on a 3-μm-thick layer of silicon dioxide on a silicon wafer.

Electrically Activated Nanocavity Laser Using One-dimensional Photonic Crystals

A. Grine, G.S. Petrich, L.A. Kolodziejski
Sponsorship: NSF MRSEC

An electrically-activated nanocavity laser that is capable of being integrated within photonic integrated circuits is being developed. The laser employs two crossed members with embedded one-dimensional photonic crystals in order to create an optical cavity at the intersection. To achieve electrical activation, one of the cross members is doped p-type and the other doped n-type. Hence, a PN-junction is formed at the intersection of the two cross members. Furthermore, one of the cross members is designed to act as a single mode waveguide. By adjusting the reflectivity of the photonic crystals, the light that is generated in the nanocavity is directed towards the output. The electrically-activated nanocavity laser is shown schematically in Figure 1.

The fabrication of the electrically-activated photonic crystal laser is underway. A mixed lithography approach is being employed; conventional contact lithography is being used for the features with dimensions greater than 1 micron while electron beam lithography is being used to define the submicron-sized features. Figure 2 shows a micrograph of the contact pads and wires for twelve lasers on the wafer that is currently being processed. The actual nanocavity portion of the lasers has not been defined yet. At the completion of the fabrication process, the nanocavity lasers will be characterized in collaboration with the Ultrafast Optics and Quantum Electronics Group.

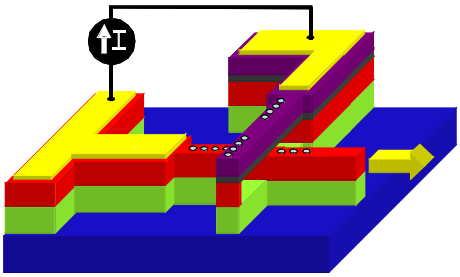

▲ Figure 1: Depiction of the electrically-activated, photonic crystal nanocavity laser. The yellow arrow represents the direction and location of the emitted light.

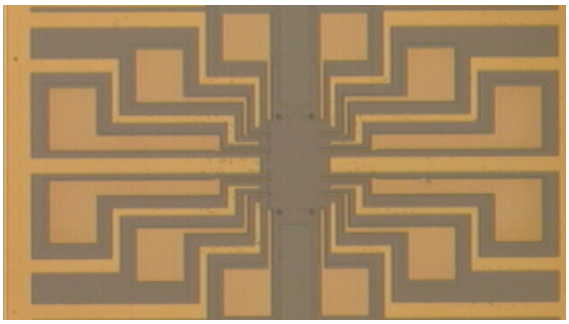

▲ Figure 2: A micrograph of the contact pads and wiring of the wafer that is currently being processed.

A Nanoelectromechanically Tunable, High-index-contrast, Interference Directional Coupler

R. Bryant, G.S. Petrich, L.A. Kolodziejski
Sponsorship: NSF MRSEC

Designs that utilize nanoprecision electrostatic mechanical actuation are likely to improve fabrication tolerances for evanescently-coupled, channel waveguide devices. Evanescent couplers, or directional couplers (DC), are notorious for their sensitivity to fabrication irregularities due mainly to the exponential dependence of the evanescent coupling on the waveguide-to-waveguide separations. A design that incorporates growth and fabrication precision as well as electromechanical nanodisplacements can significantly increase fabrication tolerances.

Molecular beam epitaxial (MBE) growth precisely defines channel waveguide heights. The MBE growth is capable of depositing homogeneous planes of material with minimal interdiffusion. Precise channel waveguide separations are achieved by a combination of atomic layer deposition (ALD) of low-index-contrast (LIC) material and nanoelectromechanical (NEM) actuation. The ALD LIC films can uniformly coat features one monolayer at a time, thus precisely defining a waveguide-to-waveguide separation with the coating thicknesses. The NEM actuation establishes intimate contact between the two ALD LIC-coated high-index-contrast channel waveguides. The NEM directional coupler waveguides are only sensitive to fabrication width variations. Optimized DC design can reduce the affect these variations have on the NEM DC.

The NEM-DC waveguides are initially set in an off-resonance state (Figure 1) and are then deflected into an on-resonance state via the application of V_0 volts (Figure 2). The initial off-resonance NEM-DC design scheme allows the waveguides to be lithographically defined as isolated features. All features can also be arranged with separations similar to the waveguide-to-waveguide off-resonances separations without having an optical loss penalty. This arrangement reduces lithographic proximity effects and loading effects associated with species diffusion-based fabrication processes (Reactive Ion Etching, and Oxidation).

Upon being deflected into an on-resonance state (V_0 volts), the two waveguides are brought into mechanically strained intimate contact. Should there be any deviations in width, the separation is preserved by the thickness of the LIC ALD coating. Depending on the application, the static power needed to preserve the strained intimate contact can be removed with the use of mechanical latches.

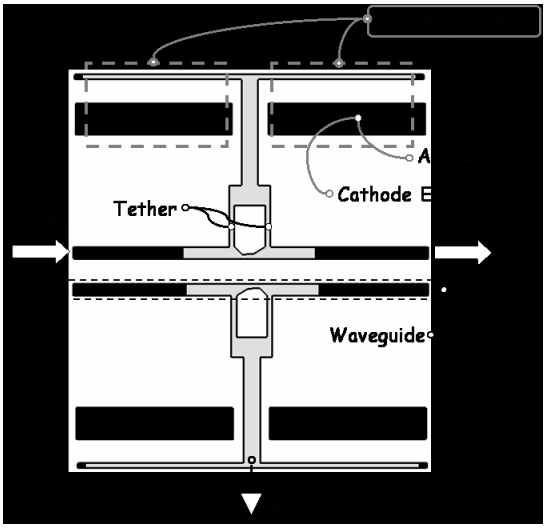

▲ Figure 1: Schematic of the directional coupler in the unpowered state. The optical signal remains in the upper waveguide.

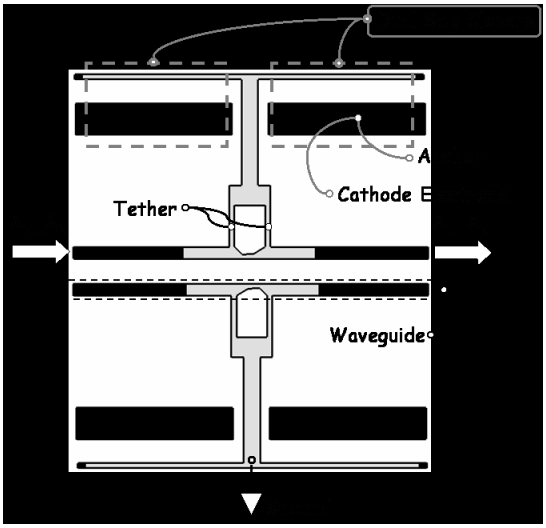

▲ Figure 2: Schematic of the directional coupler in the powered state. The optical signal is coupled into the lower waveguide.

Photonic Integrated Circuits for Ultrafast Optical Logic

R. Williams, G.S. Petrich, E.P. Ippen, R.J. Ram, L.A. Kolodziejski
Sponsorship: DARPA

The aim of this project is to model and to produce a modular monolithically-integrated, all-optical unit cell capable of performing a complete set of Boolean operations at speeds of hundreds of gigabits per second. Optical logic operations, wavelength conversion, and other advanced optical switching schemes can be implemented using the design. The basic structure consists of a balanced Mach-Zehnder interferometer (Figure 1) with an InGaAsP-based semiconductor optical amplifier in each arm. After investigation of the device design and fabrication tolerances using the beam propagation method and finite-difference time-domain (FDTD) techniques, the critical device dimensions were modeled prior to fabrication.

Fabrication processes have been developed to create the all-optical logic unit cell. The waveguide design calls for the vertical integration of passive waveguides and active amplifiers. With use of an adiabatic taper coupler (Figure 2), the optical mode is transferred between the lower passive waveguide and the upper active waveguide of the twin-waveguide structure. To minimize the amount of InGaAsP material being etched, the waveguides are placed in the center of a trench as seen in the figures. In addition to the optical logic unit cell, isolated components have been fabricated and are being tested to confirm the device design and the computer simulation results.

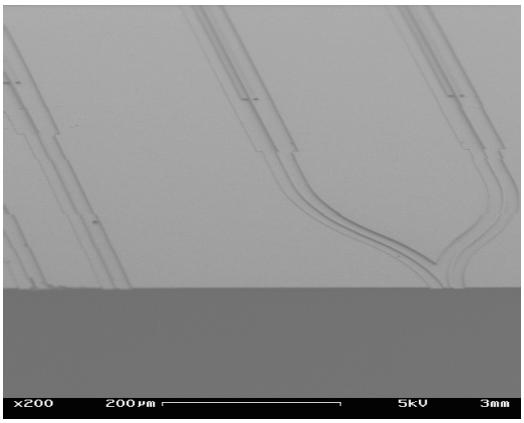

▲ Figure 1: A scanning electron micrograph of the beginning region of the Mach-Zehnder interferometer (MZI) that is the basis for the optical logic unit cell. Controlling the balance of the semiconductor optical amplifiers in each arm of the MZI permits achievement of basic Boolean functionality.

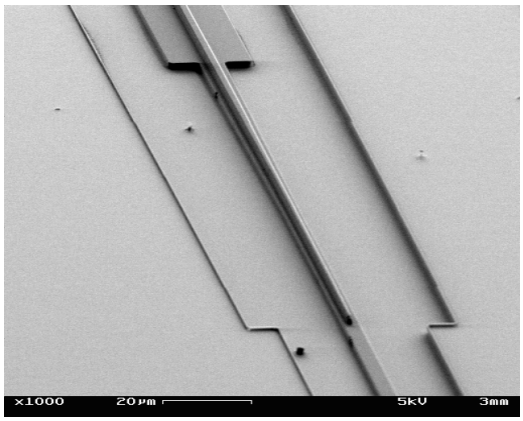

▲ Figure 2: A scanning electron micrograph showing the active waveguide taper that is used to transfer the optical mode between the lower passive waveguide (lower right) and the upper active waveguide (upper left).

Ultra-broadband Modulator Arrays

O. Shamir, G.S. Petrich, F.X. Kaertner, E.P. Ippen, L.A. Kolodziejski
Sponsorship: DARPA

Creating an arbitrary optical waveform at wavelengths that are centered at 800 nm requires an ultra-broadband modulator array. Since these modulators operate at wavelengths around 800 nm, the material choices are limited to relatively high-Al content AlGaAs and $In_{0.5}(Ga_xAl_{1-x})_{0.5}P$ layers lattice-matched to GaAs. In addition, since GaAs absorbs light with a wavelength less than 870 nm, the lower cladding layer of the modulator must be relatively thick to isolate the modulator from the GaAs substrate. To create the largest optical mode possible and to minimize the coupling loss, the index contrast between the waveguiding layers and the cladding layers should be minimized. Hence, a dilute waveguide structure in which thin layers of high index material are embedded in a low-index material is employed. The resulting layered structure has an effective index slightly higher than the low-index material and is determined by the layer thicknesses as well as the refractive index of the two materials that create the dilute waveguide.

Three slightly different structures were grown by molecular beam epitaxy: (i) an InAlP-based structure in which the dilute waveguide consisted of alternating layers of InAlP and $Al_{0.5}Ga_{0.5}As$, (ii) an $Al_{0.8}Ga_{0.2}As$-based structure in which the dilute waveguide consisted of alternating layers of $Al_{0.8}Ga_{0.2}As$ and InGaP, and (iii) an $Al_{0.8}Ga_{0.2}As$-based structure employing two AlAs layers that can be oxidized. All of the structures are challenging in terms of the epitaxial growth. In the phosphide-based structure, the growth of thick, lattice-matched InAlP cladding layers is challenging due to the need to maintain the lattice-matched condition and due to possible anion ordering. In the arsenide-based structure, although the use of $Al_{0.8}Ga_{0.2}As$ for the cladding layer minimizes the lattice mismatch problem, achieving high-quality, high-Al content AlGaAs cladding layers is difficult due to the low Al adatom mobility on the surface during growth. The third structure with AlAs layers that can be oxidized enables the optical mode to be strongly confined in the vertical direction, allows unipolar operation due to the insulating Al_xO_y layers, and allows high operating voltages to be used. To minimize free-carrier loss in the first two structures, the modulator uses a P-I-N structure in which the Si and Be dopants are graded from the contact layers to the dilute waveguide region.

The first two structures are anticipated to have similar optical mode profiles; the structures are designed to be single mode in a 2-μm-wide ridge waveguide. Using OptiBPM, the fundamental mode for the phosphide-based structure is calculated to be roughly 2 μm x 1 μm (WxH); a similar mode profile exists for the arsenide-based structure. In both structures, if the dilute waveguide is not completely etched, due to the low index contrast of the dilute waveguides, the bending radius is quite large, on the order of a millimeter. The optical mode of the third structure is calculated to be roughly 1.5 μm x 1 μm (WxH). The mode in this structure is more tightly confined due to the low-index Al_xO_y layers.

Fabrication is underway using a mask set containing Mach-Zehnder interferometer modulators of various lengths with multimode interference couplers or Y-splitters. The Mach-Zehnder interferometer modulators as well as conventional modulators are oriented both parallel and perpendicular to the major flat of the 2" GaAs (100) wafers. The mask set also contains a variety of passive components, such as Y-splitters and multimode interference couplers, as well as straight and curved waveguides.

Low-power Thermal Tuning of Second-order Microring Resonator

R. Amatya, R.J. Ram
Sponsorship: DARPA

Thermal tuning is one of the mechanisms to achieve active functionality from the ring resonators. These structures can be used as tunable filters, wavelength switches, add-drop multiplexers, converters, and modulators. Polymer waveguides have been reported with very efficient thermal tuning due to their low thermal conductivity and high thermo-optic coefficients. The InP/InGaAsP microrings fabricated with waferbonding using polymer (BCB) have been tuned with power consumption of 26μW/GHz [1]. A CMOS-compatible, SiN ring has been reported with a tuning efficiency of 20pm/K and a tuning power of 400μW/GHz [2]. We show theoretical simulation for efficient thermal tuning of SiN second-order filters using a tuning power of 60μW/GHz. This is the first attempt at such low-power, efficient thermal tuning for a high-order microring resonator.

Second-order filters are fabricated with silicon-rich SiN (n = 2.2) cores and silicon oxide (SiO_2) as a lower cladding and hydrogen silsequioxane (HSQ) as the upper and side cladding. Fabrication and design details for the resonator are described in [3]. The thermo-optic coefficient ($\Delta n/\Delta T$) is temperature- as well as wavelength-dependent. At 1.55 μm, the thermo-optic coefficients for SiN and SiO_2 are 4e-5 K^{-1} and 1.5e-5 K^{-1} respectively. The theoretical tuning range for the waveguide is calculated to be 27pm/K. Before cladding deposition, we performed initial measurements on second-order filters with air as the upper cladding using external heaters. The change in center wavelength (Figure 1) is approximately 36pm/K. Due to slight variation in the group index of the waveguide with air cladding as compared to the HSQ cladding, the experimental tuning range is different from the theoretical value.

Optimized thin film titanium heaters (100nm) are designed to sit on top of the cladding to locally change the temperature of the resonator. Finite-element thermal simulation (FEMLAB) gives the temperature profile for the filter showing approximately one-dimensional heat flow with very low thermal cross-talk. Heaters with high thermal impedance are appropriate in order to minimize power dissipation for thermal tuning. Figure 2 shows the proposed heater design along with test heater data showing thermal impedance and tuning power. The total tuning power for the finalized heater design is less than 60μW/GHz with a tuning range of 150GHz for 40K change in the ring temperature. The 3ω technique has been used to validate the thermal impedance of the test heater.

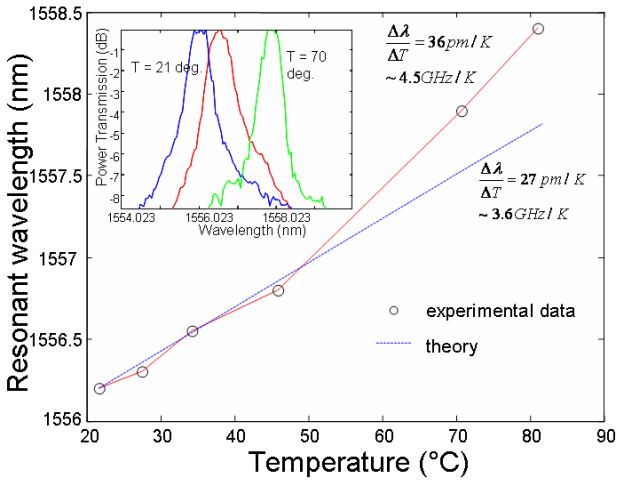

▲ Figure 1: Thermal tuning for the second-order filter is observed by changing the temperature of the rings. A total shift of 2.2 nm is seen, due to heating the rings from 21°C - 81°C. Inset shows the drop port spectra.

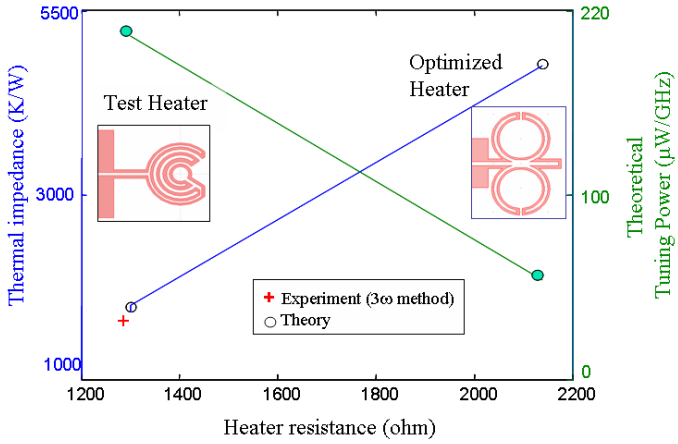

▲ Figure 2: Experimental and theoretical measurements of impedance for a test heater. Final heater design simulation shows low tuning power and high thermal impedance.

REFERENCES

[1] I. Christiaens, D. Van Thourhout, and R. Baets, "Low-power thermo-optic tuning of vertically coupled microring resonators," *Electronics Letters*, vol. 40, no. 9, pp. 560-561, Apr. 2004.

[2] D.H. Geuzebroek, E.J. Klein, H. Kelderman, F.S. Tan, D.J.W. Klunder, and A. Driessen, "Thermally tunable, wide FSR switch-based on micro-ring resonators," in *Proc. of the Symposium IEEE/LEOS Benelux Chapter*, Amsterdam, 2002. pp. 155-158.

[3] T. Barwicz, M.A. Popović, P.T. Rakich, M.R. Watts, H.A. Haus, E.P. Ippen, and H.I. Smith, "Microring-resonator-based add-drop filters in SiN: fabrication and analysis," *Optics Express*, vol. 12, no. 7, pp. 1437, Apr. 2004.

Frequency-multiplexed Fluorescence-detection Arrays in Polymer Waveguide Backplanes

K.S. Lee, R.J. Ram
Sponsorship: CMSE, Government of Malaysia

Many biochip systems require optical detection at discrete locations, such as flow cytometers, PCR chips, and bioreactors [1-3]. As these systems become more integrated and parallel, multiple fluorescence sources in various locations on-chip, often with overlapping spectra, must be detected. To provide sensors for these systems, optical detection must be made scalable, compact, and cheap, utilizing non-imaging optics such as waveguides and reducing off-chip components such as photodetectors and photomultiplier tubes. Frequency division multiplexing (FDM) has been explored as a method to reduce component costs and increase speed for multichannel fluorescence microscopes [4]. We extend this detection approach by combining waveguides with frequency multiplexing as a low-cost and scalable approach for the accurate detection of multiple fluorescence signals located within a single chip.

Figure 1 shows a schematic of the fabricated waveguide array. Four waveguides in the upper layer provide excitation to the fluorescent sources above the chip. The emission is then collected through the vertical vias and reflected into the collection waveguides. All four collected signals are then combined and detected with a single silicon PIN photodiode. To test the multiplexing capability of the system, four oxygen-sensitive lifetime-based fluorophors (PtOEPK) [5] were excited at different frequencies. The step response of each sensor was measured by exposing each sensor to a burst of nitrogen in series and measuring the fluorescence output of all sensors. As shown in Figure 2, the modulation frequency of each sensor is distinguishable and sensor responses can be measured individually with minimal cross-talk. With use of frequency multiplexing, data acquisition can be performed significantly faster with fewer detectors, a necessity for compact integrated systems.

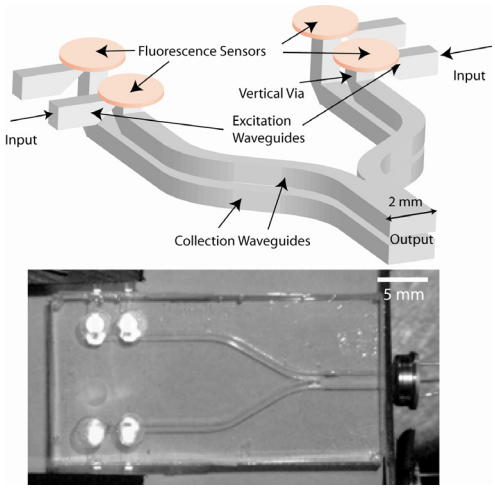

▲ Figure 1: Schematic and image of the waveguide array. Individual excitation waveguides provide different modulation frequencies to sensors located above the waveguide chip. All collected fluorescence is then routed to a single detector, minimizing the number of detection components.

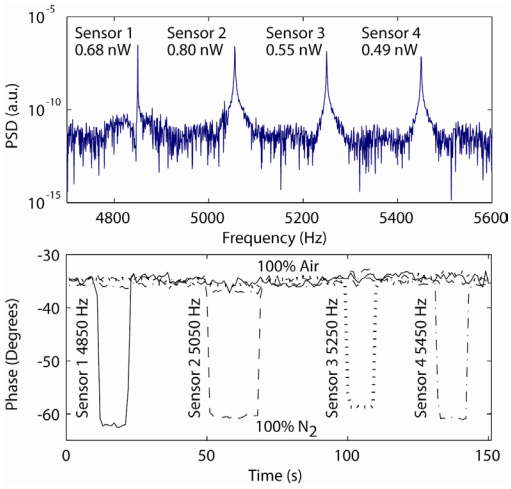

▲ Figure 2: Detected output from four different fluorescence lifetime-based oxygen sensors during nitrogen step responses. Modulated signals are spaced by 200 Hz and phase detection is performed digitally. Since the fluorescence lifetime is sensitive to oxygen, a measured phase change relates to oxygen concentration.

REFERENCES

[1] C.H. Lin, G.B. Lee, and G.L. Chang, "Micro flow cytometers integrated with buried SU-8/SOG optical waveguides," *Sensors and Actuators A*, vol. 130, pp. 165–70, Jan. 2003.

[2] J. Khandurina, T.E. McKnight, S.C. Jacobson, L.C. Waters, R.S. Foote, and J.M. Ramsey, "Integrated system for rapid PCR-based DNA analysis in microfluidic devices," *Analytical Chemistry*, vol. 72, pp. 2995-3000, July 2000.

[3] H.L.T. Lee, P. Boccazzi, R.J. Ram, and A.J. Sinskey, "Microbioreactor arrays with integrated mixers and fluid injectors for high-throughput experimentation with pH and dissolved oxygen control," *Lab on a Chip*, vol. 6, no. 9, pp. 1229-1235, Sep. 2006.

[4] F. Wu, X. Zhang, J.Y. Cheung, K. Shi, Z. Liu, C. Luo, S. Yin, and P. Ruffin, "Frequency division multiplexed multichannel high-speed fluorescence confocal microscope," *Biophysics Journal*, vol. 91, pp. 2290-2296, June 2006.

[5] D.B. Papkovsky, G.V. Ponomarev, W. Trettnak, and P. O'Leary, "Phosphorescent complexes of porphyrin ketones: Optical properties and application to oxygen sensing," *Analytical Chemistry*, vol. 67, pp. 4112-4117, Nov. 1995.

Towards Front-end CMOS-compatible Photonic Devices for High Bandwidth Density, Ultra-low-power, Core-to-Memory Communications

J.S. Orcutt, M. Popovic, F. Gan, A. Khilo, N. Dilello, J.L. Hoyt, F. Kaertner, V. Stojanović, R.J. Ram
Sponsorship: DARPA

For the past few decades, CMOS technology generation scaling has pushed forward digital electronic chips and all fields that rely upon them. Unfortunately, the overall system performance is no longer improving as rapidly, due to bottlenecks such as interconnect performance. Unfortunately, as the computing cores scale so that many can be fit onto a single chip, the electronic communication busses to supply them with information, especially to and from main memory, do not scale with the required energy and density efficiency.

One solution is to replace the electrical I/O network with an optical one. If wavelength division multiplexing (WDM) is utilized, the bandwidth per micron of chip real-estate used could be drastically improved with respect to electrical links. Additionally, since the relevant challenges for the on-chip optics are to modulate, distribute, and detect light fed in from an off-chip laser source as opposed to providing the energy to drive the capacitance of the electrical interconnect, optics has the potential to be more energy efficient [1].

The optoelectronic components then required for this link are an energy efficient modulator and photodiode. However, since the goal of this project is to replace existing electronics with optics, we are attempting to realize these components in the existing scaled CMOS layers shown in Figure 1. We have chosen to explore using the polysilicon interconnect layer as the waveguide cores for the optical busses. Therefore, the required photon energy must be below that of the silicon band edge to minimize absorption. Given this constraint, we propose using the silicon-germanium already present for strain engineering in the PFET source/drains to act as our absorber (see Figure 2 for details). Previous silicon photonics projects have already demonstrated a promising silicon modulator in a specialized process flow [2]. The remaining challenge for this project is to optimize the existing design for short reach digital communication while changing the active material from single crystalline silicon to polysilicon.

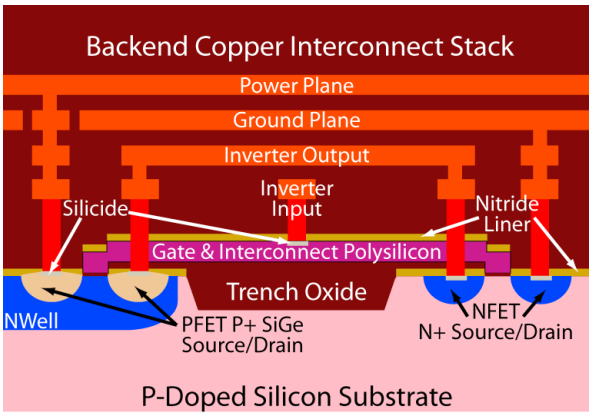

▲ Figure 1: Cross-section cartoon of a typical CMOS inverter in a scaled CMOS node. Relevant features and material layers are labeled above. The challenge for optics is to take these existing layers and use them for a new application.

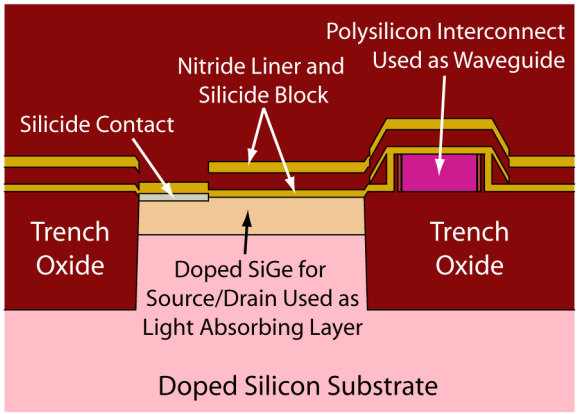

▲ Figure 2: Cross-section of a proposed silicon-germanium photodetector laterally coupled to a polysilicon waveguide. The first few layers of interconnect metal are left empty so as not to interfere with the optics.

REFERENCES

[1] T. Barwicz, H. Byun, F. Gan, M. Geis, M. Grein , C.W. Holzwarth, J.L. Hoyt, E.P. Ippen, F.X. Kärtner, T. Lyszczarz , O.O. Olubuyide, J.S. Orcutt, M.A. Popović, P.T. Rakich, R.J. Ram, H.I. Smith, S. Spector , V. Stojanović, M.R. Watts, and J.U. Yoon , "Silicon photonics for energy-efficient interconnects," *J. Opt. Net.*, to be published.

[2] F. Gan and F.X. Kärtner, "High-speed silicon electro-optic modulator design," *Photon. Technol. Lett.*, vol. 17, pp. 1007-1009, May 2005.

Magnetic Oxides for Optical Isolators and Magnetoelectronic Devices

C.A. Ross, G.J. Dionne, A. Taussig, L. Bi, V. Sivakumar, H.S. Kim
Sponsorship: Lincoln Laboratory, ISN, MicroPhotonics Consortium

We have established a thin-film laboratory that includes a pulsed-laser deposition (PLD) system and an ultra-high vacuum sputter/analysis system. In PLD, a high-energy excimer laser is used to ablate a target, releasing a plume of material that deposits on a substrate to form a thin film. The PLD is particularly useful for making complex materials such as oxides because it preserves the stoichiometry of the target material.

We have been using PLD to deposit a variety of oxide films for magneto-optical devices such as isolators. These materials include iron oxide, which can adopt one of four different ferrimagnetic or antiferromagnetic structures depending on deposition conditions, and bismuth iron garnet (BIG, $Bi_3Fe_5O_{12}$), which is useful for magneto-optical isolators in conventional photonic devices. The ideal material for an isolator combines high Faraday rotation with high optical transparency. Garnets have excellent properties but do not grow well on silicon substrates, making it difficult to integrate these materials. In contrast, iron oxide (maghemite) grows very well on MgO or Si, with high Faraday rotation but its optical absorption is high. One way to solve this problem is to develop new magneto-optical active perovskite structure materials, which grow well on MgO or $SrTiO_3$. We have examined Fe-doped barium titanate thin film (Figure 1) [1], which shows strong magneto-optical property and weak optical absorption. Recently we are also aiming to fabricate double perovskite thin film with magnetically ordered Fe sites to produce high magneto-optical properties. Epitaxial $BiFeO_3$ thin film on $SrTiO_3$ substrate has been fabricated (Figure 2), and we are trying to modify its magneto-optical property by doping. These films could be useful for waveguide isolators and other magnetoelectronic devices in which optical absorption losses are critical. A second project involves the use of electrochemical methods to control the magnetization of iron oxide spinel structure films (magnetite or maghemite) grown on conducting substrates, making a chemically-switchable material. The insertion of Li ions by electrochemical discharge changes the oxidation state of the Fe(III) to Fe(II) and can reduce the magnetization of the film by about 30%, in a reversible process. Recent experiments on nanoparticles of iron oxide show much greater changes in magnetization, up to ~80%, indicating that the process is kinetically limited.

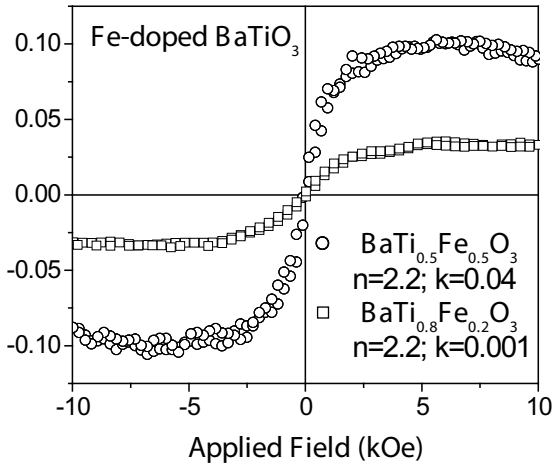

▲ Figure 1: Faraday rotation vs. applied field for 750-nm-thick $BaTi_{0.5}Fe_{0.5}O_3$ and $BaTi_{0.5}Fe_{0.5}O_3$ films grown in a vacuum on MgO substrates, with the field perpendicular to the film.

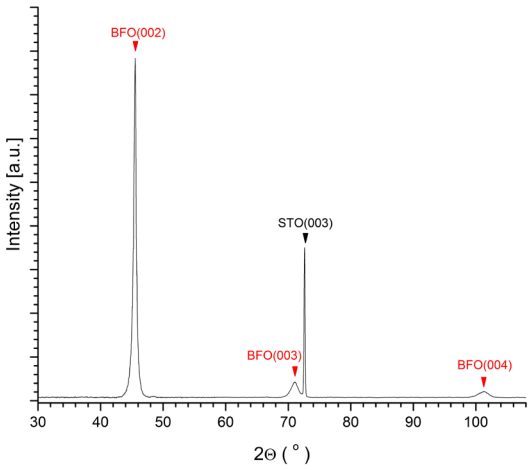

▲ Figure 2: X-ray diffraction spectrum of 260-nm-thick $BiFeO_3$ epitaxial film on $SrTiO_3$ substrate.

REFERENCES

[1] A. Rajamani, G.F. Dionne, D. Bono, and C.A. Ross, "Faraday rotation, ferromagnetism, and optical properties in Fe-doped $BaTiO_3$," *Journal of Applied Physics*, vol. 98, no. 6, pp. 063907:1-4, Sep. 2005.

Polarization-transparent Optical Add-drop Multiplexers in Silicon Nitride

T. Barwicz, M.R. Watts, M.A. Popovic, P.T. Rakich, C.W. Holzwarth, E.P. Ippen, F.X. Kaertner, H.I. Smith
Sponsorship: Pirelli S.p.A, internal funds

Microphotonics promises to revolutionize optics through miniaturization and dense integration of optical elements on planar surfaces. Of particular interest are microphotonic devices that employ high refractive-index contrast (HIC). These devices have dimensions on the order of the optical wavelength and functionality often not achievable with macro-scale devices. A long-standing criticism of HIC microphotonic devices, however, is their inherent sensitivity to polarization; i.e., they respond differently to light polarized along different axes. Since the polarization state changes randomly in optical fibers, HIC microphotonic devices are incompatible with the optical fibers necessary to connect them to the outside world.

In the NanoStructures Laboratory, we have developed techniques that enable the fabrication of microphotonic devices, such as microring-based filters, that have unprecedented dimensional accuracy, resulting in unprecedented optical performance. In addition, we have overcome the problem of sensitivity to polarization by means of an integrated polarization-diversity scheme that renders the optical response of HIC microphotonic devices and systems insensitive to polarization. An optical add-drop multiplexer was realized and the polarization-dependent loss reduced to an average of 1 dB [2]. Figure 1 presents the optical circuit diagram implemented, the optical response, and electron micrographs of the structure. The waveguides are fabricated in silicon-rich silicon nitride, and the critical dimensions vary from 70 to 3000 nm. The average waveguide widths of the 18 microrings forming the add-drop multiplexer are matched to 0.15 nm. The aspect ratio of the tallest and thinnest structures reaches 12 to 1.

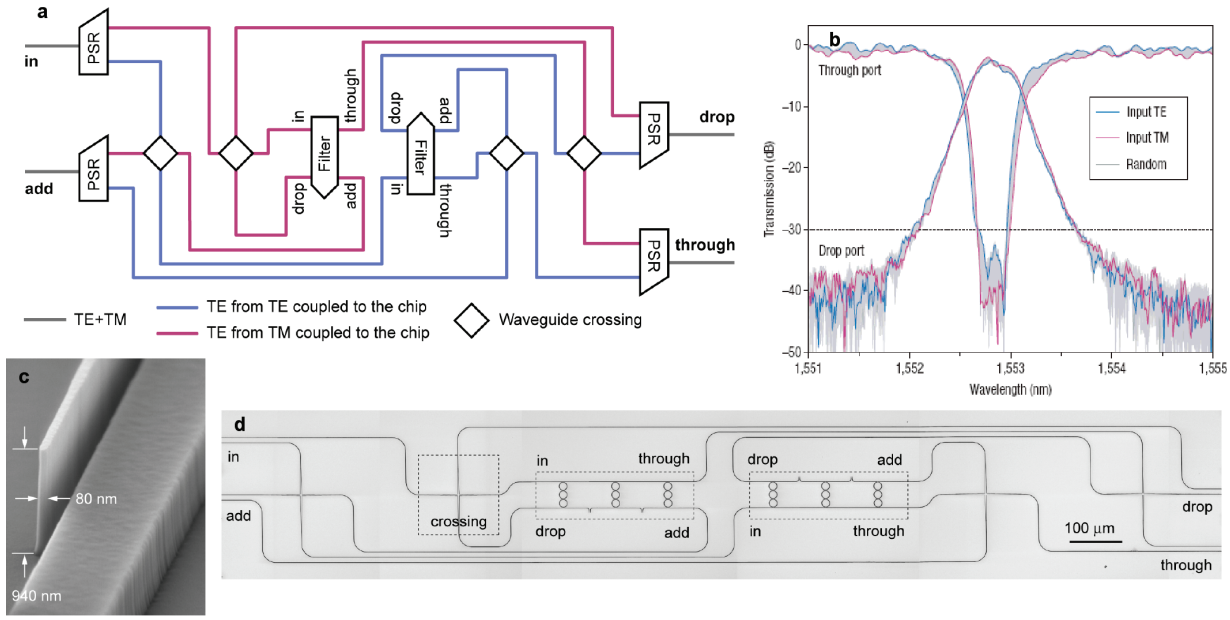

▲ Figure 1: (a) Optical circuit required to obtain a polarization -nsensitive optical response from polarization-sensitive components. The acronym PSR stands for polarization splitter and rotator. The two filters shown in the schematic are identical. (b) Device response with a mean polarization dependent loss of 1 dB. (c) Electron micrograph of the beginning end of the polarization splitter and rotator. (d) Optical micrograph of the middle part of the circuit. The polarization splitters and rotators, which are not shown, extend to the right and the left of the micrograph. The grayscale was inverted to allow the fine lines to be readable when printed.

REFERENCES

[1] T. Barwicz, M.A. Popovic, M.R. Watts, P.T. Rakich, E.P. Ippen, and H.I. Smith, "*Fabrication of add-drop filters based on frequency-matched microring-resonators*," *Journal of Lightwave Technology*, vol. 24, pp. 2207-2218, May 2006.

[2] T. Barwicz, M.A. Popovic, M.R. Watts, P.T. Rakich, L. Socci, E.P. Ippen, F.X. Kartner and H.I. Smith, "*Polarization-transparent microphotonic devices in the strong confinement limit*," *Nature Photonics*, vol. 1, pp. 57-60, Jan. 2007.

Fabrication of Nanostructured Optical Fiber-to-chip Couplers

R. Barreto, M. Defosseux, T. Barwicz, A.M. Khilo, M. Fan, M.A. Popovic, P.T. Rakich, M. Dahlem, C.W. Holzwarth, E.P. Ippen, F.X. Kaertner, H.I. Smith
Sponsorship: DARPA

Efficient fiber-to-chip coupling is a significant problem for high-index-contrast (HIC) microphotonics due to the large difference in size and refractive index between the core of an optical fiber (several micrometers in diameter) and the core of a HIC waveguide (less than one micrometer wide). An efficient fiber-to-chip coupler is thus needed to match the mode of the fiber and transform it to a propagating mode within the HIC waveguide. We investigated two different approaches to accomplish the efficient coupling. In the first design, called a horizontal coupler, a large polymer waveguide, with a mode diameter that nearly matches the mode diameter of an optical fiber, sits on a small silicon waveguide whose width tapers from 30 to 450 nm. This taper allows the optical power to be transferred adiabatically from the polymer waveguide to the silicon waveguide. Figure 1 shows a three-dimensional view of the horizontal coupler design. Fabrication is done on silicon-on insulator wafers, so that the buried oxide functions as an undercladding, preventing optical modes from extending into the substrate. With only slight modifications, this design can be made compatible with overclad photonic devices. The second design, the vertical coupler, is based on a grating array composed of nanoscale elements that allow coupling from a vertically oriented fiber to a horizontally oriented waveguide. We are currently demonstrating this concept using silicon-rich silicon-nitride waveguides. Figure 2 shows a sketch of the vertical-coupler design. The minimum feature size is ~100 nm.

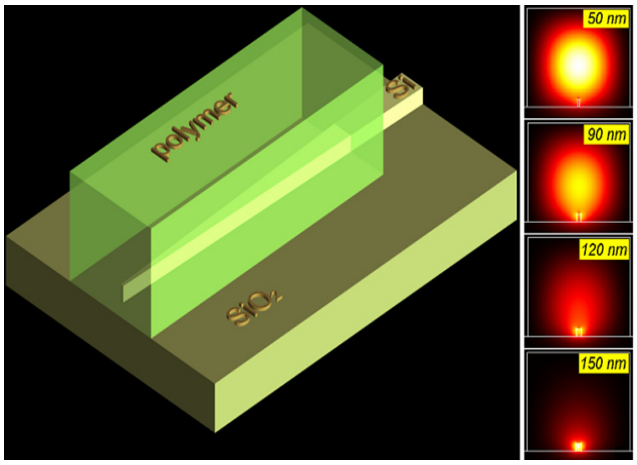

▲ Figure 1: Three-dimensional view of horizontal coupler.

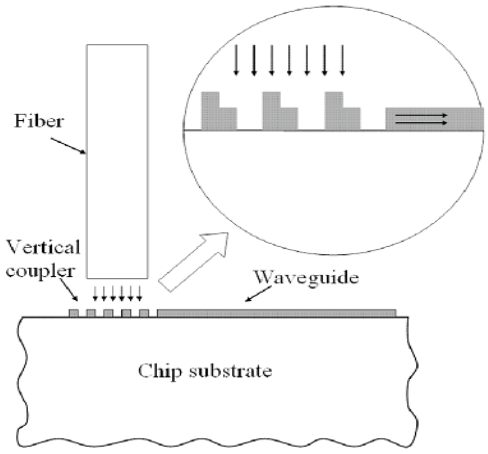

▲ Figure 2: Sketch of a vertical coupler.

A $BaTiO_3$-based Electro-optic Thin-film Waveguide Modulator

J. Hiltunen, D. Seneviratne, H.L. Tuller (in coll. with J. Yasaitis)
Sponsorship: Analog Devices

The drive towards integrated photonics requires the integration of various optical devices on a chip including an optical modulator. Currently, optical modulation with active waveguiding structures is implemented using $LiNbO_3$ single crystals. These devices require complex and expensive fabrication processes. In addition, their relatively low electro-optic coefficient leads to large component sizes, limiting miniaturization. The current demands for an increased degree of integration with cost-efficient device fabrication can, in principle, be met using thin films of barium titanate [1-3]. In bulk form, this material possesses a superior electro-optic coefficient. Applications using thin-film structures necessitate careful study of processing parameters and their impact on material properties. Our efforts are geared towards gaining a fundamental knowledge of the behavior of thin film barium titanate ($BaTiO_3$) and developing processes to fabricate devices for applications in optical data transmission and processing.

The focus is on optimizing the electro-optic response of $BaTiO_3$ and related thin-film materials deposited by pulsed laser deposition (PLD) and sputtering onto single-crystal substrates directly or with buffer layers. Figure 1 shows a cross section of a waveguide Mach-Zehnder interferometer structure, using a SiN strip-loaded waveguide. The optical waveguide structure is formed by growing a Si_xN_y layer with plasma-enhanced-chemical-vapor-deposition (PECVD) on $BaTiO_3$ and patterning it lithographically. This is followed by the sputtering and patterning of Al electrodes next to one arm of the Mach-Zehnder structure. The operation of the interferometer is characterized by launching polarized light into the waveguide and measuring the modulation of the output intensity as a function of applied voltage. A typical DC response of a sample electro-optic modulator based on barium titanate is shown in Figure 2. We have demonstrated an effective electro-optic coefficient as high as 85pm/V with $BaTiO_3/SrTiO_3$ superlattices, which is considerably greater than that available with bulk $LiNbO_3$ crystals.

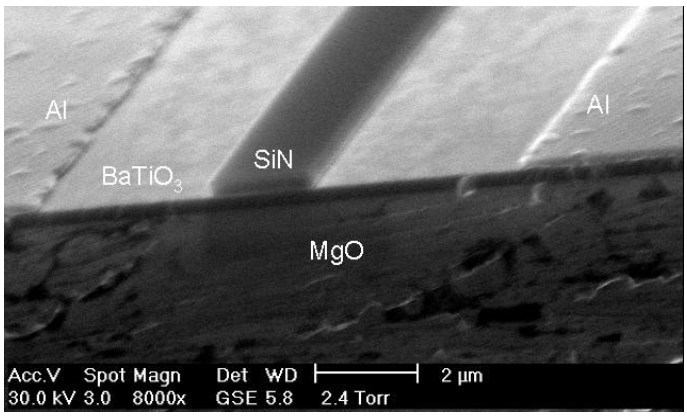

▲ Figure 1: Cross section of the Mach-Zehnder waveguide modulator.

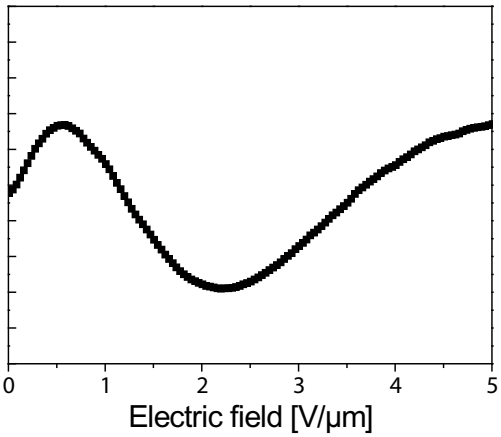

▲ Figure 2: Measured optical intensity at the Mach-Zehnder waveguide modulator output as a function of electric field between adjacent electrodes.

REFERENCES

[1] A. Petraru, J. Schubert, M. Schmid, and C. Buchal, "Ferroelectric $BaTiO_3$ thin-film optical waveguide modulators," *Applied Physics Letters*, vol. 81, no. 8, pp. 1375-1377, Aug. 2002.

[2] D.M. Gill, C.W. Conrad, G. Ford, B.W. Wessels, and S.T. Ho, " Thin-film channel waveguide electro-optic modulator in epitaxial $BaTiO_3$," *Applied Physics Letters*, vol. 71, no. 13, pp. 1783-1785, Sep. 1997.

[3] P. Tang, A.L. Meier, D.J. Towner, B.W. Wessels, "$BaTiO_3$ thin-film waveguide modulator with a low voltage-length product at near-infrared wavelengths of 0.98 and 1.55 µm," *Optics Letters*, vol. 30, no. 3, pp. 254-256, Feb. 2005.